



Tailoring surface defects in Plasma Electrolytic Oxidation (PEO) treated 2-D black TiO₂: Post-treatment role, and intensification by peroxyomonosulfate activation in visible light-driven photocatalysis

Reza Hosseini ^a, Arash Fattah-alhosseini ^{a,*}, Minoo Karbasi ^{a,*}, Stefanos Giannakis ^{b,*}

^a Department of Materials Engineering, Bu-Ali Sina University, Hamedan 65178-38695, Iran

^b Universidad Politécnica de Madrid (UPM), E.T.S. de Ingenieros de Caminos, Canales y Puertos, Departamento de Ingeniería Civil: Hidráulica, Energía y Medio Ambiente, Unidad docente Ingeniería Sanitaria, c/ Profesor Aranguren, s/n, ES-28040 Madrid, Spain



ARTICLE INFO

Keywords:

Oxygen vacancy (OV)
Plasma electrolytic oxidation
Tetracycline (TC)
Photocatalytic activity
PMS activation

ABSTRACT

Herein, we have developed a visible light-responsive black TiO₂ photocatalytic coating with controlled formation of oxygen vacancies (OV) and Ti³⁺ species, crucial for enhancing photocatalytic reactions. The rational control of these semiconductor defects was achieved through plasma electrolytic oxidation (PEO), followed by NaOH post-treatment. The coating's effectiveness was evaluated by tetracycline (TC) degradation. The surface defects function as traps, reducing electron/hole recombination and forming mid-gap/localized-donor states, narrowing the band gap. Rigorous material characterization confirmed unaffected morphology and PEO coating phases, while increasing the density of OVs and Ti³⁺ species. As a result, TC photo-degradation was ~3.5 times higher compared to plain PEO coatings. The material demonstrated exceptional stability and efficiency, while it was successfully intensified via peroxyomonosulfate (PMS) activation, leading to high synergies (2.10). Scavenger tests revealed the existence of both radical/non-radical pathways, indicating the prevailing photocatalytic mechanism and the key differences achieved through this novel process.

1. Introduction

Sulfate radical-based advanced oxidation procedures (SR-AOPs) have gained much interest lately for environmental protection and/or remediation [1,2]. Among the different oxidants that can induce them, like peroxyomonosulfate (PMS) and peroxydisulfate (PDS), PMS gains increasing preference, since it can be activated easier, due to its asymmetrical structure, and its ability to produce SO₄²⁻ and HO[•] at the same time [3]. Besides, compared to conventional AOPs, the SO₄²⁻ produced have a long half lifetime (30–40 µs for SO₄²⁻ vs. 20 ns for HO[•]), higher stability and notable oxidation potential (2.5–3.1 V and 1.8–2.7 V vs. NHE for SO₄²⁻ and HO[•], respectively), while possessing the capability to perform effectively at a wide range of pH [4,5]. To generate these oxidizing species, numerous techniques are available, such as UV irradiation, heat, ultrasound, metal ions, as well as metal oxide-based semiconductors, including TiO₂, Bi₂MoO₆ under visible UV irradiation, or even visible light [6–8].

Heterogeneous photocatalysis is a non-selective and highly effective process for the elimination of organic contaminants, easy to use, with

possible catalyst recycling. Hence, at the lab scale, it has been proven to be a potent method for degrading a broad range of water pollutants [9]. Among semiconductors, due to their non-toxicity, widespread availability, low cost, thermal and chemical stability, and biologically and chemically inert character, TiO₂ is the most widely used commercial photo-catalyst [10–13]. Among the different crystallite structures of TiO₂, the photocatalytic activity (PA) of TiO₂ is derived from rutile and anatase crystal phases [14]. There are intrinsic problems in the application of powder semiconductors as photo-catalysts (upscale, reactors' costs, etc.) but as every process that is in its infancy (compared to a mature technology, e.g., ozonation), it is expected to overcome these issues at some point and achieve their application. As a result, adopting photocatalytic coatings of surfaces as an alternative to suspended powder application may promote the recovery of photo-catalysts, industrialization capacity, and reusability at several stages [15–17]. Although there are several methods to produce photocatalytic TiO₂-based coatings [18], due to the prolonged exposure and the need to reuse the coatings in photocatalytic applications, the likelihood of leaching from the substrate is relatively high; in turn, the coating's

* Corresponding authors.

E-mail addresses: a.fattah@basu.ac.ir (A. Fattah-alhosseini), m.karbasi@basu.ac.ir (M. Karbasi), stefanos.giannakis@upm.es (S. Giannakis).

adherence to the substrate is one of the primary issues associated with using photocatalytic coatings [19]. Preparing coatings by Plasma Electrolytic Oxidation (PEO) has been a useful approach for achieving excellent adhesion and metallurgical bonding of the coating to the substrate [20]. Additionally, PEO is a promising strategy for fabricating porous surfaces with a high specific surface area and with high PA, as well as creating the anatase and rutile TiO_2 crystalline phases at a relatively low process time and room temperature [21,22].

To overcome the low photocatalytic quantum efficiency and broad band gap of TiO_2 [23], band gap engineering, such as the introduction of surface defects including Ti^{3+} species, OV states, and surface hydroxyl (-OH) groups, known as TiO_{2-x} or black TiO_2 , are among the most promising methods for expanding the absorption range to improve the efficiency of PA under visible light [24–30]. In addition to reducing the edge of the valence band (VB), achieving optimal OV concentration could generate mid-gap/localized-donor states just under the conduction band (CB). In contrast, the existence of Ti^{3+} elevates the localized excitation of the Ti^{3+} ions via 3d transitions from the gap state to the empty excited state [31]. It is worth mentioning that both phenomena can significantly reduce the band gap, increase its light absorption, and thus enhance the photocatalytic properties of TiO_{2-x} under visible light [28,29]. Furthermore, these energy levels can operate as a trap, reducing or delaying the rate of electron-hole recombination and ultimately enhancing PA [32].

As an effective way of PA increase, there are a variety of methods for introducing OVs into TiO_2 , including heat treatment under oxygen discharge conditions involving vacuum [33], hydrogen [34–36], and neutral gas [37] atmospheres, metal- or non-metal ion doping [38,39], and chemical reduction [40–46]. Although thermal treatment by hydrogen gas has been extensively utilized to introduce oxygen vacancies (OV) in TiO_2 , the easy-to-apply and inexpensive chemical reduction method has piqued the interest of researchers in recent years, in the effort to overcome the risks of hydrogen thermal treatment.

Despite that the majority of black TiO_2 generated is in powder form [41, 44], a simple and low-cost strategy was developed to introduce OVs into supported TiO_2 anodized coating, by chemical reduction in a diluted NaBH_4 solution, as a strong and common reducing agent [40,45,46]. The obtained results exhibited that TiO_{2-x} coating has an optimum morphology, increased Fermi-level, reduced effective work function, and amended conductivity in comparison to plain TiO_2 anodizing coating. Since NaBH_4 use is connected to work safety issues, OV development using NaOH chemical reduction is a more secure solution, as well as low-cost [47–49]. Liu et al. [49] successfully synthesized OV-decorated Bi_2WO_6 through a NaOH alkali etching process. The results exhibited that the light absorption capability of deficient $\text{Bi}_2\text{WO}_{6-x}$ is highly magnified, and the separation rates of photo-generated carriers are augmented in comparison to pure Bi_2WO_6 . However, so far, the NaOH -reducing agent has not been reported to create OVs on TiO_2 nanoparticles and coatings.

Since antibiotics are a known environmental problem, it would be interesting to assess the possibility of applying OV-rich PEO-treated TiO_2 toward their elimination from aqueous matrices. As such, this work focuses on the removal of TC, the second most-produced antibiotic in the world, under visible-light photocatalytic removal mediated by these coated materials.

The newly developed materials were fully characterized and showed promising potential in their use as photo-catalysts. The degradation of TC as a model bio-recalcitrant contaminant, mediated by the post-alkali-treated PEO coatings was assessed, alongside the impact of different photocatalytic process parameters, including TC concentration and pH. Based on the experimental findings and the use of scavengers, the occurring photocatalytic mechanism of TC degradation was proposed. Finally, the TC degradation efficiency by intensification of the process via optimal coating/peroxymonosulfate (PMS) under visible light was evaluated, and the overall integrated pathways for the optimal coating-mediated photocatalytic activation of PMS and the subsequent TC degradation were proposed.

2. Materials and methods

2.1. PEO coating preparation

Pure Ti was used (Grade 2, 99.9 wt%) as substrate, with dimensions of $20 \times 15 \times 1 \text{ mm}^3$. The PEO experiment was conducted utilizing a commercial pulsed DC power supply apparatus, in a phosphate-based electrolyte mixture of trisodium phosphate ($\text{Na}_3\text{PO}_4 \cdot 12 \text{ H}_2\text{O}$, 5 g/l, Merck, Germany) and potassium hydroxide (KOH , 4 g/l, Merck, Germany). Also, the chosen electrical parameters, namely the current density, duty cycle, and frequency were 6 A/dm^2 , 80%, and 1000 Hz, respectively. Finally, the treatment time was set at 10 min, and the produced coating was named PEO.

2.2. Post-alkali treatment of produced PEO coatings

Modified alkali etching was considered to produce coatings with different amounts of OVs [49–51]. Briefly, PEO coating was immersed in different concentrations of sodium hydroxide (at the range of M, e.g., 2 M NaOH , Merck, Germany) aqueous solution as a reducing agent and magnetically stirred for various times (at the range of hours, e.g., 16 h) at room temperature (RT). Post-alkali-treated PEO coatings were washed with double de-ionized water and then introduced in hydrochloric acid solution (HCl , 0.1 M, Merck, Germany) for 1 h and washed with distilled water again to produce the PEO coatings containing different amounts of OVs. The related information about the post-alkali-treated PEO coatings and the sample codes is given in Table 1. The two-step procedure for producing PEO coatings with different amounts of OVs is shown in Fig. 1. Also, to study the surface-OH groups' effect on the PA, the optimum coating (RT-2 M-16 h sample) was placed in a vacuum oven at 120°C for 6 h and named RTO-2 M-16 h.

As mentioned in the introduction section, to compare our process with the different established methods for introducing surface OVs on the PEO coating, two common methods were assessed as controls, namely: hydrogen thermal treatment of the PEO was carried out in a tube furnace with a hydrogen flow of 100 mL min^{-1} for 3 h at 500°C [33] and chemical reduction via NaBH_4 as a reducing agent [40].

2.3. Coating characterization

X-ray diffraction (XRD, AW-XDM300) using $\text{CuK}\alpha$ (1.5406 \AA) radiation was utilized to analyze the phase composition and crystal structure of both the PEO and post-alkali-treated PEO coatings. The XRD patterns were analyzed with Xpert Highscore software based on the standard ICDD database to identify the phase. Moreover, the XRD data was subjected to Rietveld refinement using the Materials Analysis Using Diffraction (MAUD) software. To analyze the microstructures of the PEO coatings before and after post-alkali treatment, the surface morphology and elemental composition studies are conducted by FE-SEM (QUANTA 200 FEI-working at 30 kV) outfitted with an energy-dispersive spectrometer (EDS, Silicon Drift 2017). The static wettability of the PEO and post-alkali-treated PEO coatings was done by a CAM (Contact Angle Measuring) tool. Wettability measurements for each coating were conducted three times.

Table 1

Sample codes and the parameters of post-alkali-treated PEO coatings.

Sample code	NaOH concentration (M)	Post-alkali treatment duration (h)
RT-1 M-16 h	1	16
RT-2 M-16 h	2	
RT-3 M-16 h	3	
RT-4 M-16 h	4	
RT-2 M-8 h	2	8
RT-2 M-24 h		24

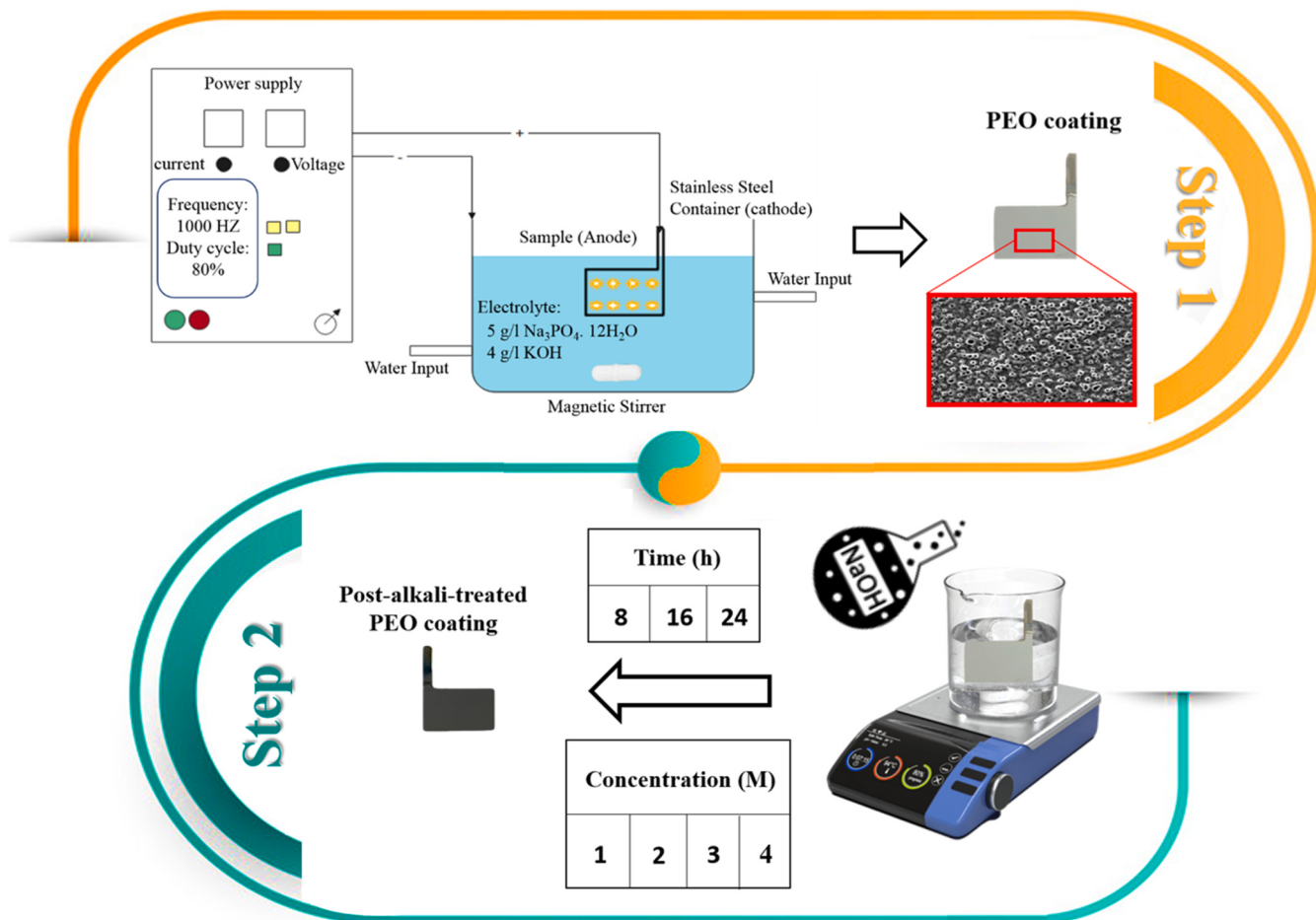


Fig. 1. Schematic of the PEO coating production with different amounts of OV.

A Perkin Elmer Lambda 25 spectrophotometer equipped with a Cd-He laser was utilized as the excitation source to obtain the photoluminescence (PL) spectrum of both the PEO and post-alkali-treated PEO coatings. The laser operated at a wavelength of 325 nm. A UV-Vis diffuse reflectance spectrometer (DRS, Shimadzu) was utilized to determine the optical parameters of the coatings, including absorbance and band gap energy. The laser Raman spectroscopy experiments were conducted using a TakRam N1-541 spectrometer equipped with an Ar-ion laser emitting at a wavelength of 532 nm. The Mott-Schottky analysis was performed in a 3.5 wt% NaCl aqueous solution using a three-electrode cell setup at a frequency of 1000 Hz. The counter electrode was made of platinum, the working electrode consisted of the coated sample and the reference electrode utilized was Ag/AgCl. The coatings' composition was examined using an Omicron X-ray photoelectron spectroscopy (XPS) device at room temperature. The analysis utilized a non-monochromatic Mg K α excitation source with an energy of 1253 eV. When calibrating the binding energy, the C 1 s level at 284.6 eV was chosen as the internal standard. XPS lines of Ti 2p and O 1s were recorded. Spectral deconvolution was accomplished using CasaXPS software.

2.4. Photocatalytic activity

Tetracycline (Purity=98%, Sigma-Aldrich, USA) degradation at room temperature was used to evaluate the PA of coatings. In this regard, the coatings with an active area of 3 cm² were immersed into 30 mL of a 15 mg.L⁻¹ aqueous TC solution and were exposed to visible light. As a visible light source, a 100-W commercial visible LED lamp

(10,959 lm, 380 nm < λ < 780 nm) with an irradiance of 540 mW/cm² on the solution's surface (Fig. S1) was utilized. Before the photocatalytic measurements, the TC adsorption-desorption equilibrium on the PEO coating was evaluated in the dark. Moreover, TC was examined for photolysis upon visible light without a photo-catalyst. High-performance liquid chromatography (HPLC, 1260 Infinity, Agilent Co.) with an Agilent Eclipse XDB-C18 column and a column temperature of 50 °C was used to assess the collected TC concentration at various time intervals. To evaluate the concentration of TC, 60% acetonitrile and 40% deionized water with 0.1% phosphoric acid (all from Merck, having a purity of 99.9 wt%) were utilized as the mobile phase at a flow speed of 1.0 mL min⁻¹, and the detection wavelength measured 280 nm. The mineralization of TC was also evaluated by the total organic carbon (TOC) analytical instrument (TOC-V CPH). Moreover, the chemical oxygen demand (COD) was measured by the closed reflux colorimetric analysis (COD Reactor AL38, Germany). To identify the intermediate products from the degradation of TC, liquid chromatography-mass spectrometry (LC-MS, 6460 LC/QQQ, Agilent Co.) was used. The photocatalytic degradation of TC with or without PMS (Oxone, 2KHSO₅·KHSO₄·K₂SO₄, 99.95%, Sigma-Aldrich Co.) was calculated according to the following Eq. 1:

$$\%PA = \frac{C_0 - C}{C_0} \times 100 \quad (1)$$

Where C (mg.L⁻¹) is the TC concentration at time t (h) after irradiation and C₀ (mg.L⁻¹) represents the primary TC concentration. Moreover, to investigate the photo-produced reactive intermediates (PPRIs) during TC photo-degradation on the optimal post-alkali-treated PEO coating,

scavengers such as isopropanol (IPA), ethylenediaminetetraacetic acid disodium (EDTA-2Na), sodium azide (NaN_3), chloroform (CHCl_3), sodium pyruvate ($\text{C}_3\text{H}_5\text{NaO}_3$), ethanol (EtOH), and tert-butyl alcohol (TBA) (all from Merck, with a purity of 99.9 wt%) were used. Also, to confirm the main active species during the photo-degradation process, the electron spin resonance (ESR) signals of the radicals that were spin-trapped by DMPO (5,5-Dimethyl-1-pyrroline N-oxide, Sigma-Aldrich, USA) were recorded on a paramagnetic spectrometer (ESRA-300, Bruker Co.). Additionally, other photocatalytic factors, such as the concentration and pH of the TC solution were systematically evaluated.

3. Results and discussion

3.1. Phase analysis of PEO and post-alkali-treated PEO coatings

In Fig. 2(a), the XRD patterns of the PEO and post-alkali-treated PEO coatings are shown. During the PEO process, the semi-stable rutile phase of TiO_2 is formed at a temperature of around 600–800 °C [52]. Therefore, the peaks of crystalline phases of anatase (ICDD card No. 01-083-2243) and rutile (ICDD card No. 01-078-1509) were detected

in all patterns. In addition, due to the low thickness and porosity in the PEO coatings, X-rays simply penetrated the titanium substrate, and peaks of Ti (ICDD card No. 00-044-1294) were discovered in all the patterns of XRD.

By performing XRD Rietveld refinements with the aid of MAUD software, it was possible to determine quantitatively the identification of the PEO and post-alkali-treated PEO coatings crystalline phases, as shown in Fig. 2(b) and (c). Since the concentration of NaOH in the post-alkali treatment at room temperature did not affect the percentage of crystalline phases, the normalized weight percentages of TiO_2 phases in the PEO and post-alkali-treated PEO coatings (RT-2 M-16 h) were tabulated in Table S1.

From the enlarged view of the 24–27° range (Fig. 2(a)), the diffraction peak of the post-alkali-treated PEO coatings shifted slightly to a high angle as compared to the PEO coating [53–56]. According to Bragg's law, the peak shift towards higher angles shows a low inter-planar distance, indicating that the lattice parameters decrease, which may arise from the presence of OVs in the TiO_2 or defective TiO_{2-x} [31,57]. Also, the more significant shift of the diffraction peak of anatase (101) positioned at 25.8 in the RT-4 M-16 h coating indicates

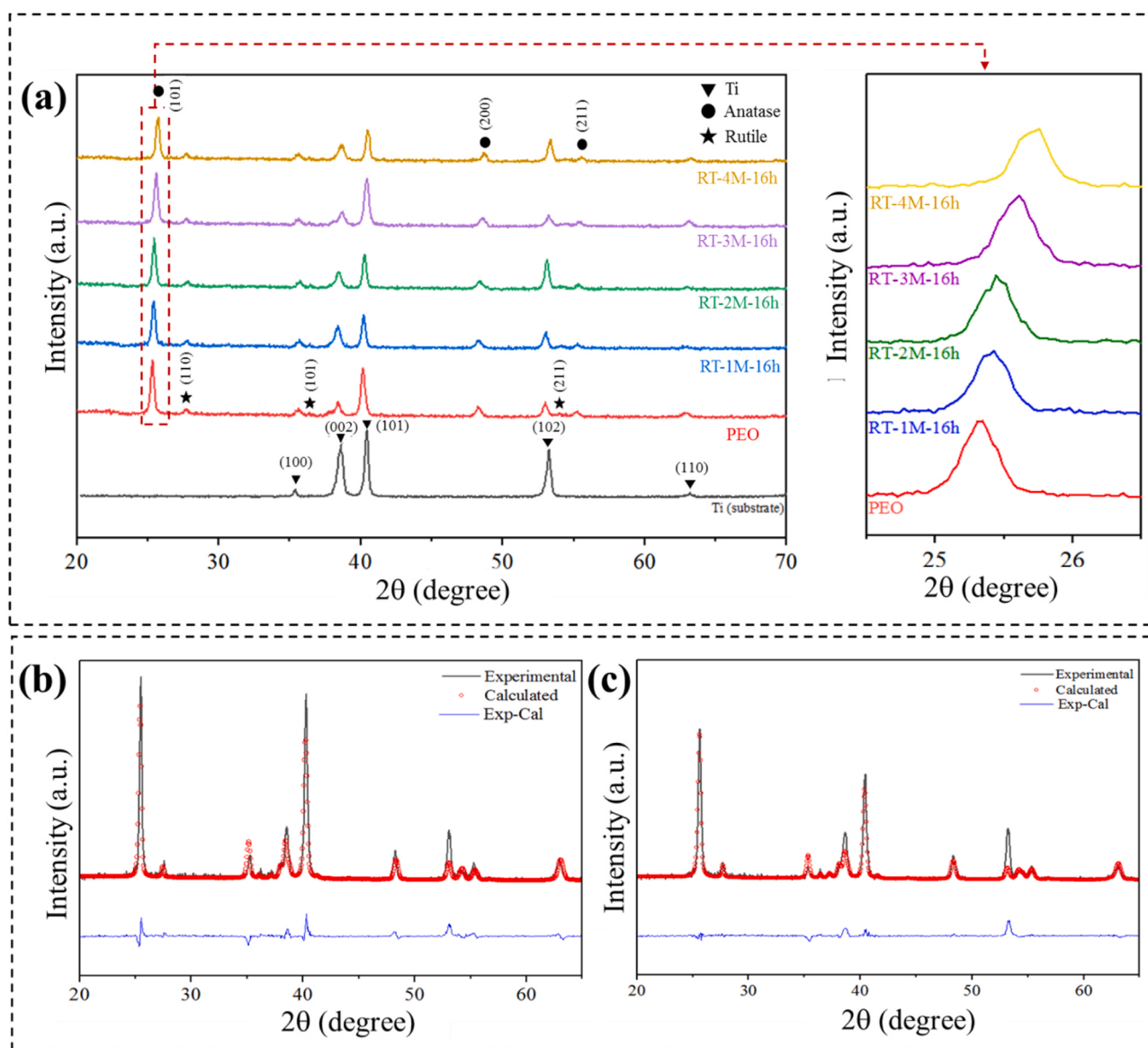


Fig. 2. (a) XRD patterns of the coatings and substrate; Rietveld refinement of the XRD pattern of the (b) PEO and (c) post-alkali-treated PEO coating by MAUD software (calculated-dots, experimental-line, and difference-bottom).

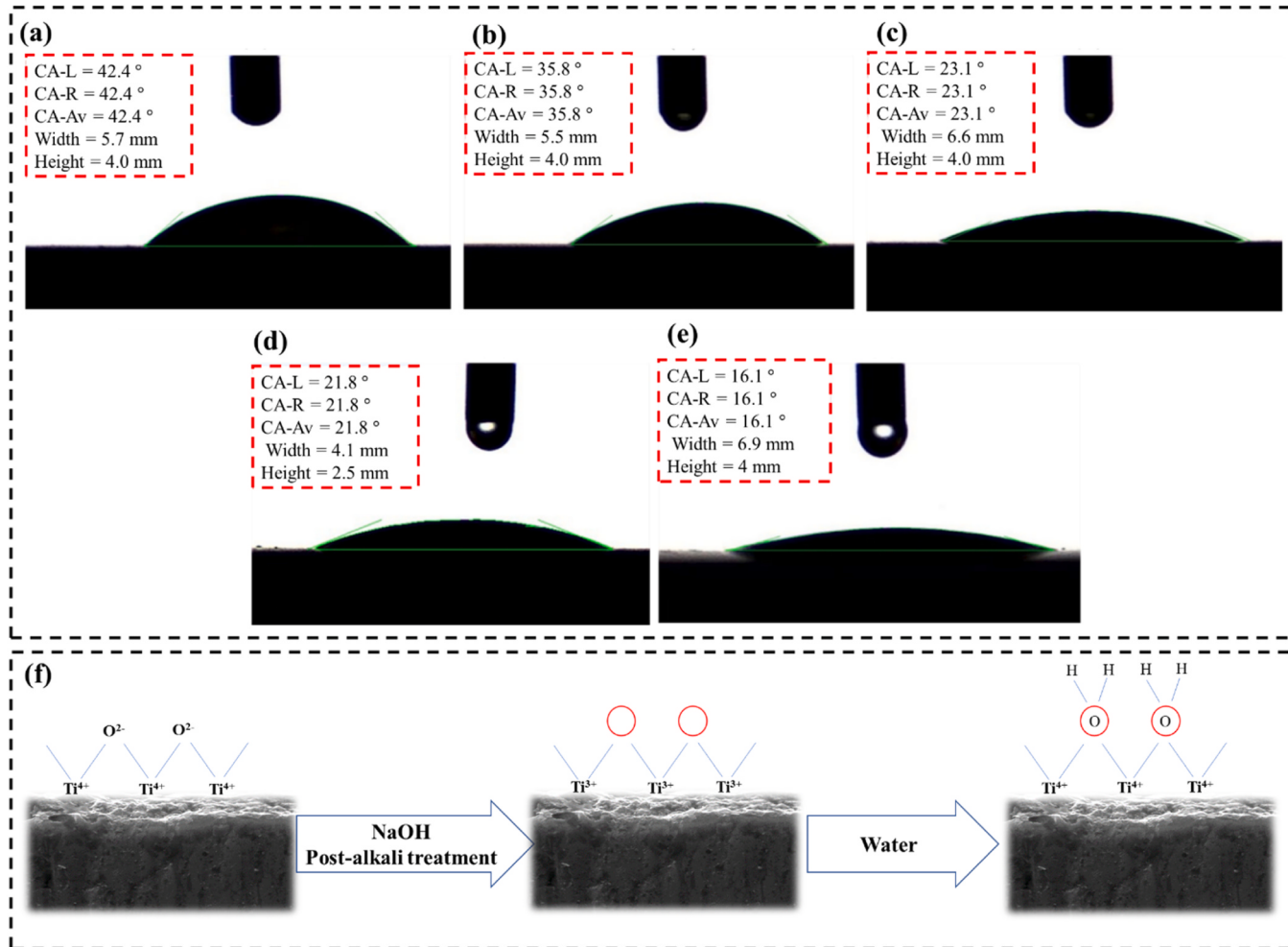


Fig. 3. Water contact angle of the (a) PEO, (b) RT-1 M-16 h, (c) RT-2 M-16 h, (d) RT-3 M-16 h, (e) RT-4 M-16 h coatings, (f) The proposed mechanism of OV-induced hydrophilicity on a post-alkali-treated PEO coating.

the formation of more OVs in TiO_2 , in accordance with other similar work [57].

3.2. Wettability of PEO and post-alkali-treated coatings

Since hydrophilicity can play a key role in the photocatalytic process, contact angle measurement was performed to assess the changes in the wettability of coatings. The results obtained from the contact angle measurement for the PEO and post-alkali-treated-PEO coatings were shown in Fig. 3(a)-(e). The contact angles of PEO and post-alkali-treated PEO coatings were less than 90° (16.1° to 42.4°), confirming the PEO coatings' hydrophilicity due to their intrinsic porosity and the presence of anatase and rutile phases. As a result of the changes in topography, the porosity of PEO coatings has a significant impact on how water spreads over the surface, namely the formation of pores, which function as capillaries for liquid within the pores. Moreover, the PEO procedure forms a surface full of the polar OH^- and O^{2-} groups owing to interactions between the plasma arc, the electrolyte, and the consist of the decomposed products of the electrolyte [58].

NaOH alkali treatment on PEO coating reduced the contact angle and made the coating more hydrophilic. Based on density functional theory (DFT) calculation, Yang et al. [59] indicated that the presence of OVs (Ti^{3+}) on the surface of TiO_2 could decrease the hydroxyl adsorption energy, resulting in a higher level of water absorbency and lower contact angle. Thus, it can be concluded that the greater hydrophilicity of the

RT-4 M-16 h coating is caused by a higher concentration of OVs (Ti^{3+}), which would be fruitful in TC photodegradation.

Moreover, as the concentration of NaOH increases in the post-alkali treatment, the hydrophilicity of the produced coating increases thanks to the transformation of Ti^{4+} sites to Ti^{3+} sites [40,42]. As schematically illustrated in Fig. 3(f), oxygen deficiency can transfer its additional couple of electrons to the adjacent two Ti^{4+} atoms to form Ti^{3+} . Consequently, the Ti-O bond is weakened and can be broken to react with chemisorbed water, resulting in the formation of two new hydroxyl groups singly bonded to each Ti atom and a consequent more hydrophilic state [60,61].

3.3. Photocatalytic activity of PEO and post-alkali-treated PEO coatings upon visible light illumination

According to Fig. 4(a), the RT-2 M-16 h exhibited the highest photodegradation efficiency of TC; about 91.52% of TC molecules were degraded within 6 h (Table S2), while the PEO coating only decomposed 50% of TC under the same experimental conditions. TC removal efficiency over different photocatalytic coatings in the dark was shown in Fig. S2. TC photocatalytic degradation could be fitted to pseudo-first-order kinetics and the Langmuir–Hinshelwood model (Eq. 2 and Fig. S3) [62–64]:

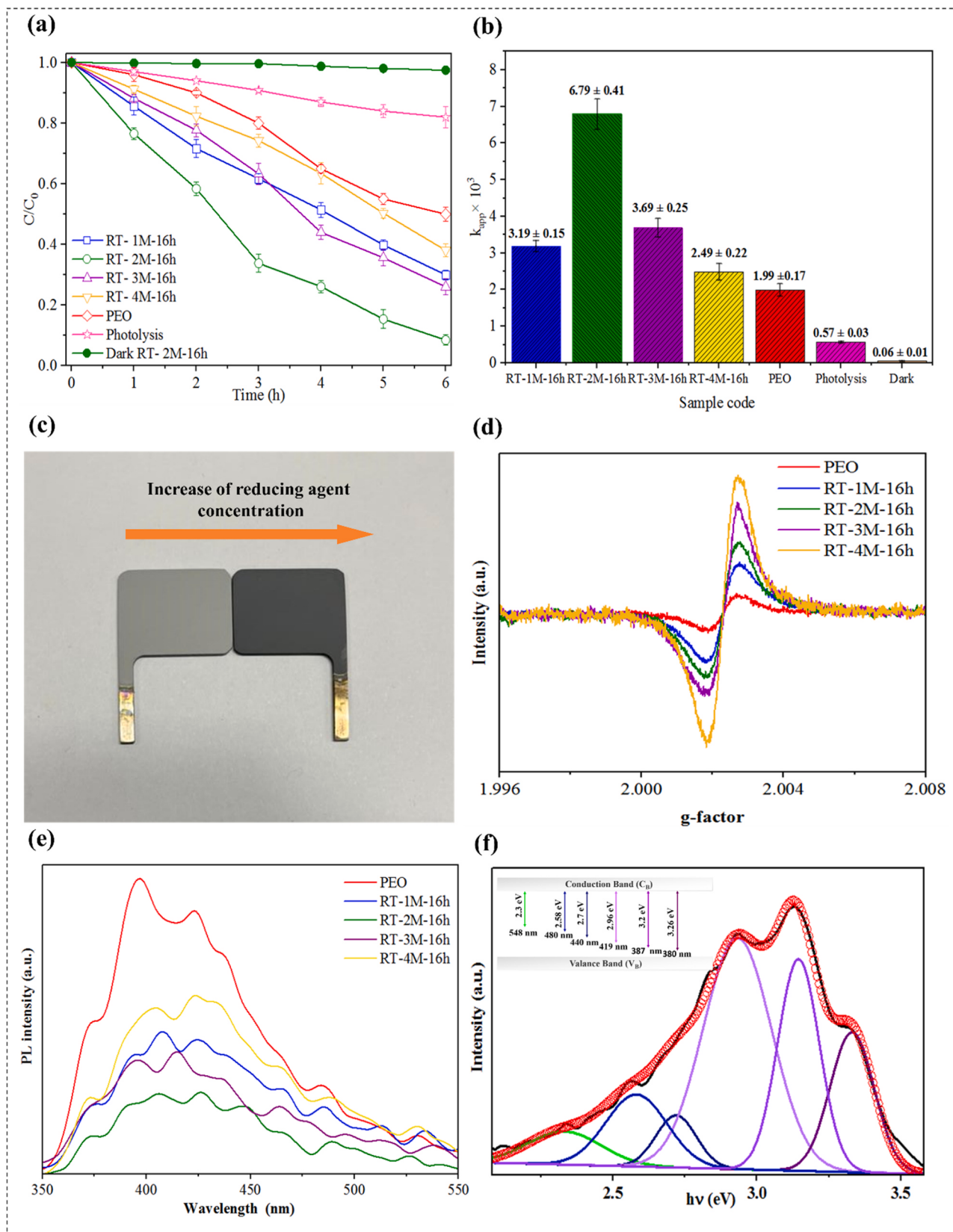


Fig. 4. (a) Photocatalytic degradation of TC upon visible light illumination over the PEO and post-alkali-treated PEO coatings, experimental conditions: light intensity = 540 mW/cm², [TC] = 15 mg.L⁻¹, and pH = 7.2, (b) Apparent reaction rate constants for the degradation of TC (c) The color change of post-alkali-treated PEO coatings from gray to black by introducing OVs, (d) EPR spectra of the PEO and post-alkali-treated coatings, (e) Photoluminescence spectra of the PEO and post-alkali-treated PEO coating, (f) The deconvolution for the PEO and schematic of energy band diagram.

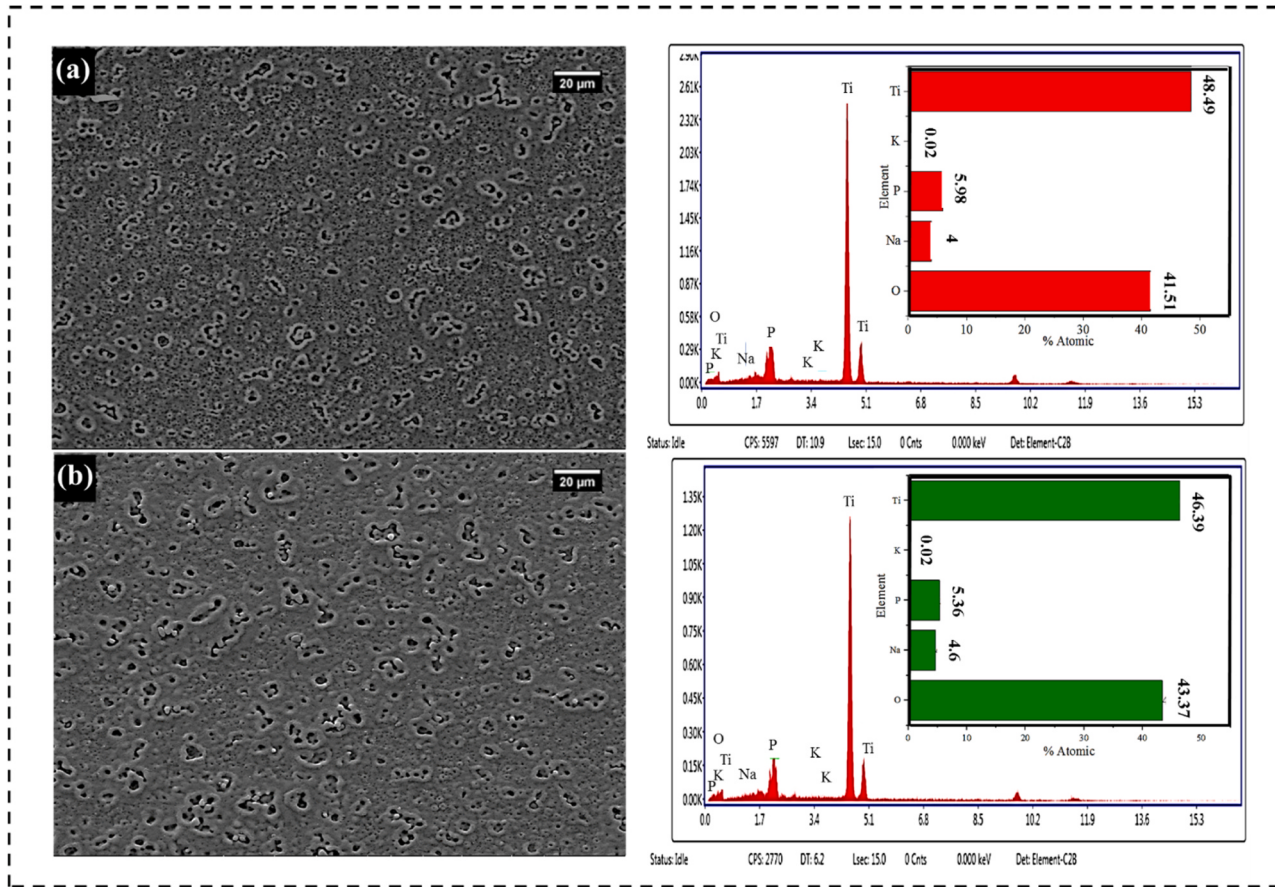


Fig. 5. FE-SEM images along with the corresponding EDS elemental spectra of (a) PEO and (b) RT-2 M-16 h (The EDS results are summarized in the inset).

$$\ln \frac{C}{C_0} = -k_{app}t \quad (2)$$

Where t is the illumination time, and k_{app} represents the pseudo-first-order degradation rate constant. Table S2 displays k_{app} and corresponding linear correlation coefficient ($Adj\text{-}R^2$), as well as the percentage of TC degradation in 6 h for the produced coatings.

According to Fig. 4(b), all the post-alkali-treated PEO coatings with different NaOH concentrations have a superior photocatalytic efficiency than the PEO coating due to a lower contact angle of the OV containing post-alkali-treated coatings, facilitating the spread of pollutants and promoting easier reactions between electrons and holes with organic compounds [65,66].

It is worth noting that the concentration of the reducing agent in the chemical reduction of TiO_2 is a crucial factor, affecting the PA of post-alkali-treated coatings [44,49]. Moreover, as seen in Fig. 4(c), by increasing the concentration of the reducing agent, the color of post-alkali-treated PEO coatings changes from light gray to dark gray or black for the PEO and RT-2 M-16 h coatings respectively, confirming the difference in the amount of OVs [44,67]. To probe the presence of OVs of the PEO and post-alkali-treated PEO coatings, electron paramagnetic resonance (EPR) was performed, leading to the paramagnetic signal centering at $g = 2.0023$ assigned to the OV trapped electrons (Fig. 4(d)) [30,68]. The rise in EPR signal intensity with increasing NaOH concentration in post-alkali treatment implies that the amount of OVs on the surface of the post-alkali-treated PEO coatings can be easily developed. For this matter, the degradation rate constant increased about 3.41 times with increasing NaOH concentration in alkaline treatment up to 2 M, which was the peak/optimal concentration. When the amount of NaOH used in the alkali treatment was increased to 4 M, a decrease was seen in the degradation rate constant.

The PL emission spectra are not only useful for providing insights into the electron-hole recombination rate in photocatalytic coatings but also for obtaining information such as surface OVs and defects [69,70]. Fig. 4(e) indicates the PL spectra of the PEO and post-alkali-treated PEO coatings with 325 nm excitation wavelength. To scrutinize the nature of defect states in the PEO coating, the deconvolution of the PL spectrum was performed (Fig. 4(f)). The first peak at about 380 nm (3.26 eV) corresponds to the band edge transitions [71]. Additionally, the emission bands near 387 nm (3.2 eV) and 419 nm (2.96 eV) reflect the characteristic free exciton emission of TiO_2 [72,73]. Moreover, the peak at about 480 nm (2.58 eV) is attributed to the surface states like $\text{Ti}^{4+}\text{-OH}$ [72]. Another emission band near 548 nm (2.3 eV) and 440 nm (2.7 eV) can be associated with defect transitions. The defect transition may be stemmed from localized surface OVs [64,73].

Surface OVs could play the role of separator for the photo-excited electron-hole pair and improve photocatalytic performance [74–76]. It is noteworthy that among different coatings, the RT-2 M-16 h coating consistently delivered the lowest PL intensity (Fig. 4(e)), indicating that the most optimized defect (OVs and Ti^{3+}) level in this coating enhances charge-carrier mobility and the redox activities [26,54,77], in agreement with the photocatalytic activities of coatings (Fig. 4(a) and (b)). Meanwhile, excessive OVs in the RT-3 M-16 h and RT-4 M-16 h coatings are proved by EPR analysis (Fig. 4(d)) can become bulk material defects [41,67], acting as charge recombination centers and suppressing charge transfer, as confirmed in the PL results [78–80]. Thus, the optimal level of OVs in post-alkali-treated PEO coatings stemmed from the balance between their dual roles as a donor source and trap sites [41,67,80]. Moreover, DFT calculation indicated that when OV concentration is too high, the maximum electron transition energy increases, and the promotion effect of OVs on photocatalytic activity is weakened [81]. This could be the reason the photocatalytic activities of the RT-3 M-16 h and

RT-4 M-16 h coatings were reduced.

As the 2 M concentration of NaOH was selected as optimal, then the impact of immersion times on the photocatalytic efficiency was also evaluated, within the 8–24 h range. According to Fig. S4(a) and (b), the increase of immersion time from 8 to 16 h resulted in the TC photo-degradation increment, but when the time increases more than the optimal immersion time, the photocatalytic degradation decreases.

3.4. Microstructure analysis and oxygen vacancy evaluation of the optimal coating

Fig. 5(a) and (b) show the FE-SEM images along with the corresponding EDS elemental analysis of the plain PEO and RT-2 M-16 h coatings. As seen in Fig. 5(a) and (b), post-alkali treatment at room temperature did not affect the morphology of the PEO coating, leading to a similar microstructure of the RT-2 M-16 h coating. The PEO and RT-

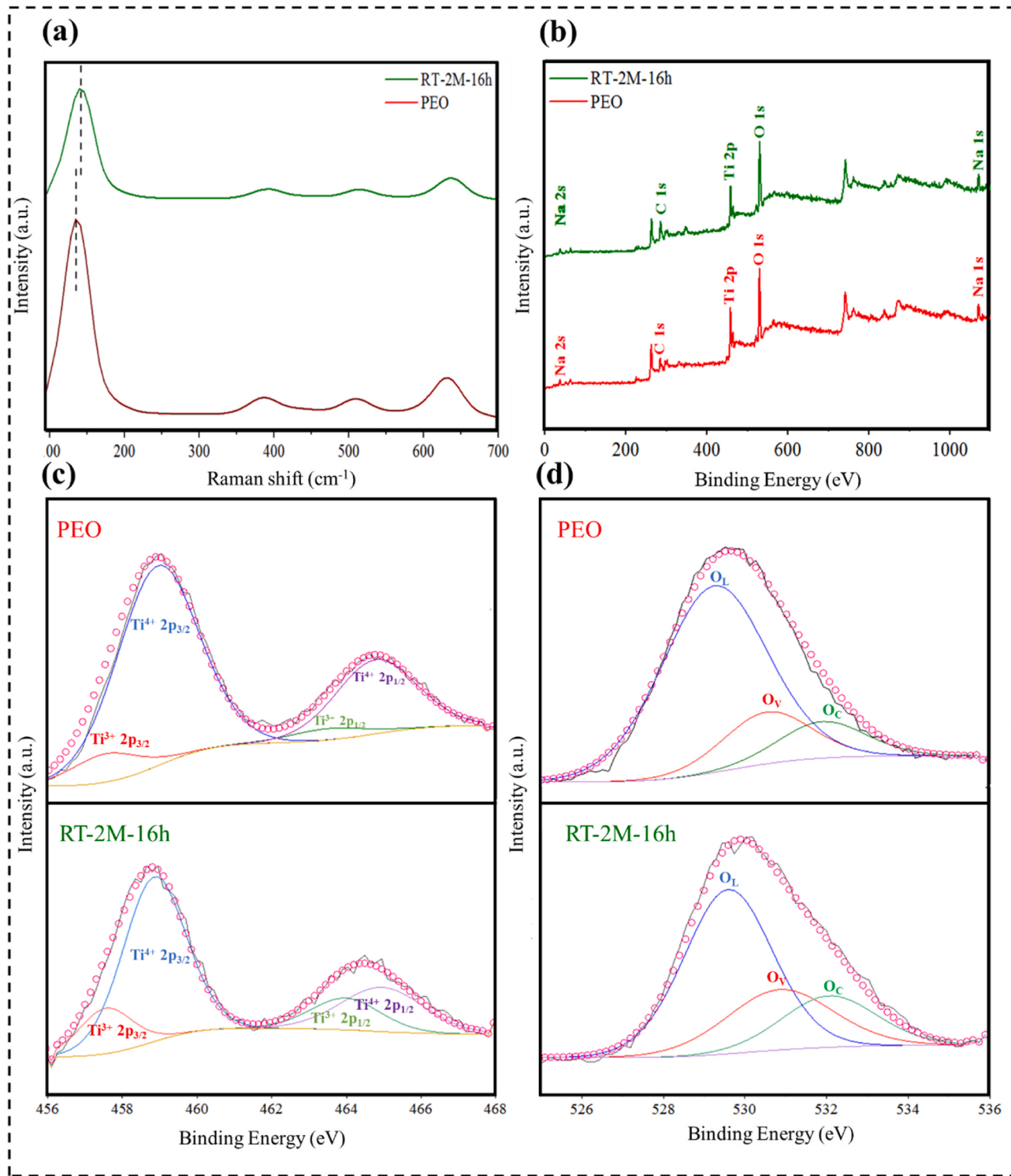


Fig. 6. (a) Raman spectra of the PEO and RT-2 M-16 h coating, (b) XPS survey spectrum of the PEO and RT-2 M-16 h coatings, Deconvolution of High-resolution (c) Ti 2p and (d) O 1 s XPS spectra of the PEO and RT-2 M-16 h coatings.

Table 2

The percentage of integrated areas of the high-resolution Ti 2p and O 1 s XPS spectra of the PEO, RT-2 M-16 h, and RTO-2 M-16 h coatings.

Peaks		Area%		
		Plain PEO	RT-2 M-16 h (post-alkali PEO)	RTO-2 M-16 h (-OH groups removed)
Ti 2p	Ti ⁴⁺	89.04	75.25	74.66
	Ti ³⁺	10.96	24.75	25.34
O 1 s	Ti-O (O _L)	71.92	56.71	62.76
	Oxygen vacancy (O _V)	16.59	24.76	25.37
	Hydroxyl group - OH (O _C)	11.49	18.53	11.87

2 M-16 h showed a typical PEO coating surface morphology, with abundant pores of various sizes and shapes homogeneously distributed on the coatings' surface. The high-energy sparks developed during PEO can increase local temperature and pressure in discharge areas, which can cause localized melting of materials. Following that, gas can be ejected from the discharge channel and be released through the coating material's molten state before quickly solidifying to create the porous structure [82–84].

The EDS results revealed that the coatings predominantly consisted of oxygen (O), titanium (Ti), and phosphorus (P) as the major elements;

Ti and O stemmed from the titanium substrate and electrolyte. Eq. 3 suggests that the existence of the phosphorus (P) element in the coating is a result of the adsorption of PO_4^{3-} ions.



Also, the existence of Na element can be originated from NaOH alkali treatment or electrolyte composition. Moreover, Eq. 4 shows that the small amounts of K element in the coating come from the ionization of KOH salt into the electrolyte [82].

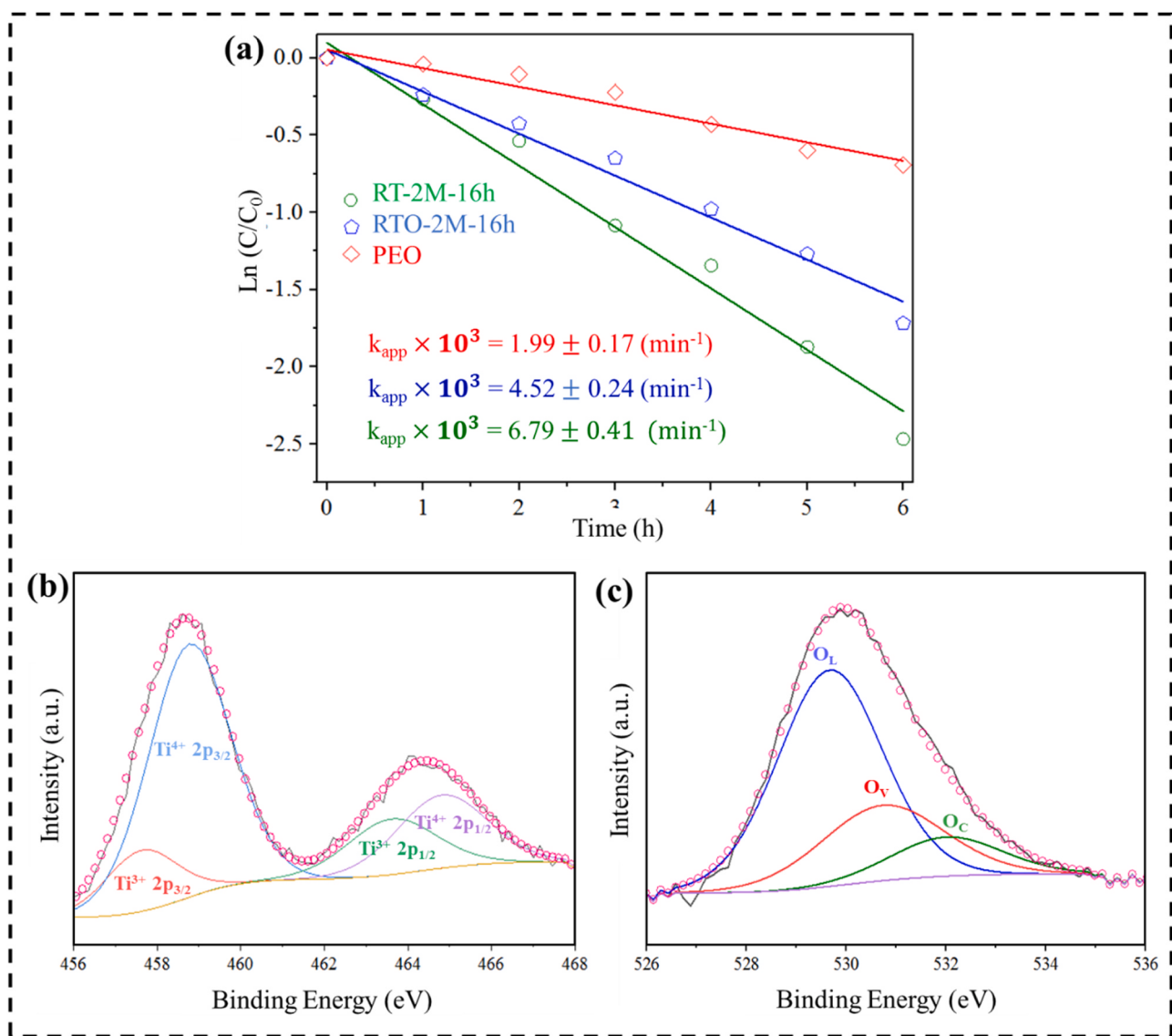


Fig. 7. (a) Reaction kinetics of TC photo-degradation over the PEO, RT-2 M-16 h, and RTO-2 M-16 h coatings upon visible light illumination. Experimental conditions: light intensity = 540 mW/cm², $[TC]_0 = 15 \text{ mg.L}^{-1}$, and pH = 7.2; Deconvolution of high-resolution (b) Ti 2p and (c) O 1 s XPS spectra of the RTO-2 M-16 h coating.

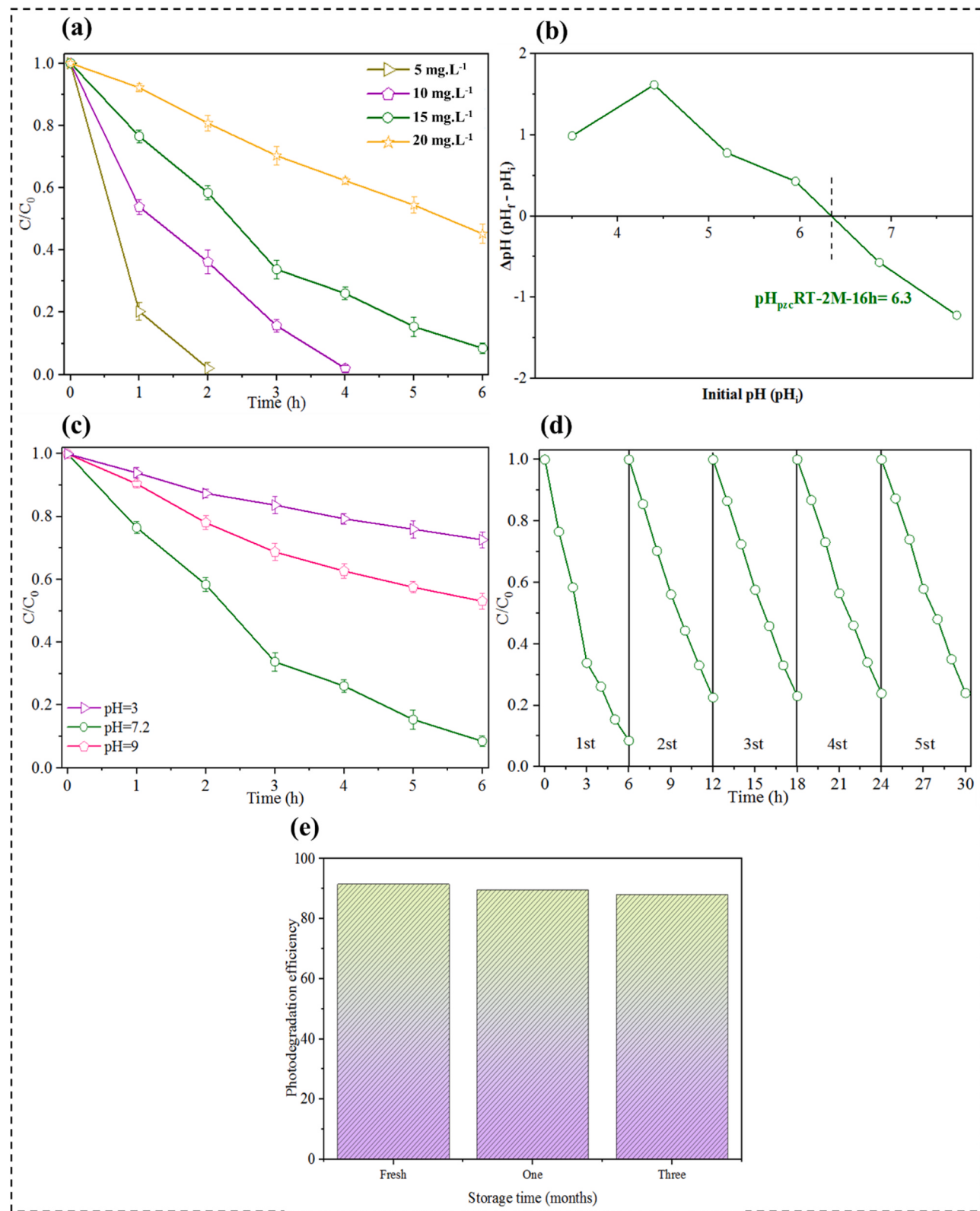


Fig. 8. (a) Impact of different initial TC concentrations over the RT-2 M-16 h, experimental condition: light intensity = 540 mW/cm², pH = 7.2; (b) Point of zero charge (PZC) of the RT-2 M-16 h estimated via pH drift technique, (c) Effect of different pH of the TC solution, Experimental condition: [TC]₀ = 15 mg.L⁻¹, light intensity = 540 mW/cm² (d) Recycling experiments of photocatalytic degradation of TC over optimal post-alkali-treated PEO coating under visible light irradiation (e) Photocatalytic degradation efficiency with different storage time for the RT-2 M-16 h under visible light illumination. Experimental conditions: light intensity = 540 mW/cm², [TC]₀ = 15 mg.L⁻¹, and pH = 7.2.



The Raman spectra for the plain PEO and the post-alkali-treated optimal coating are depicted in Fig. 6(a). Both coatings were crystalline and indicated 141, 392, 513, and 634 cm⁻¹ peaks attributed to the Eg, B1g, A1g+B1g, and Eg vibrational modes of the anatase phase, respectively [58,85]. It is interesting to note that the Raman spectrum of the optimal coating shows significant differences compared to the PEO coating. Firstly, the strongest Eg mode of the PEO coating may shift to higher frequencies in the RT-2 M-16 h coating due to localized defects or non-stoichiometry lattice disorder related to OVs and/or Ti³⁺ [53,54,86,87]. Secondly, the oxygen deficiencies (OV and Ti³⁺) cause changes in the numbers of atomic coordination and Ti-O-Ti network bonding length in the RT-2 M-16 h coating. Thus, the intensity of Raman peaks is expected to decrease as the Ti³⁺/Ti⁴⁺ molar ratio increases.

These two characteristics evidenced the rise in defects of Ti³⁺ and OV in the lattice structure of the PEO coating's surface after NaOH post-alkali treatment [54,88].

Fig. 6(b) shows the XPS full survey spectra of PEO and optimal post-alkali-treated PEO coatings. Peaks from O 1 s, Ti 2p, Na 1 s, Na 2 s, and C 1 s (C is from extraneous carbon support) were identified in the XPS spectra. Fig. 6(c) shows the high-resolution spectra of the Ti 2p for PEO and optimal coating. As revealed, the two major peaks of Ti 2p_{3/2} and Ti 2p_{1/2} can be fitted into four peaks. The 457.7 and 463.6 eV peaks are ascribed to the Ti³⁺ 2p_{3/2} and Ti³⁺ 2p_{1/2}, the 458.6 and 464.8 eV peaks are assigned to the Ti⁴⁺ 2p_{3/2} and Ti⁴⁺ 2p_{1/2}, respectively [89].

Moreover, Fig. 6(d) indicates the core-level spectra of O 1 s for the PEO and optimal coatings in which the 529.8, 530.7, and 531.9 eV peaks are, due to Ti-O bonds (O_t), oxygen defects (O_v) consisting of intrinsic defects of crystals and/or the introduced OVs accompanied Ti³⁺ species; the hydroxyl groups are a result of the contact with surface-adsorbed water (O_c) [68,90]. It is noteworthy that the presence of the O_v peak in the PEO coating O 1 s spectrum can be attributed to the rapid melting and solidification of materials during electrical micro-discharges,

$$FoM = \frac{\text{Conversion efficiency}(\%)}{\text{Catalyst mass(mg)} \times \text{initial pollutant concentration(ppm)} \times \text{Irradiation time(min)} \times \text{Applied power(W)}} \quad (6)$$

resulting in the formation of defects, including OVs, in the crystalline structure of the TiO₂ lattice [64].

The percentage of integrated areas related to each species in the Ti 2p, and O 1 s core levels is summarized in Table 2. The RT-2 M-16 h coating shows an increase of Ti³⁺ species while the concentration of Ti⁴⁺ species decreases due to the creation of OVs [28] after the post-alkali treatment of PEO coating.

Meanwhile, semiquantitative analysis of the chemical state of the RT-2 M-16 h and PEO coatings was conducted in terms of O 1 s XPS spectra. A decrease of 15.21% in the integrated areas of the Ti-O curve was observed after post-alkali treatment. Moreover, the increment in the percentage of O_v and O_c in the post-alkali-treated PEO coating can be ascribed to the higher generation of TiO_x defects. The Ti³⁺ molar proportion was calculated at 24.75% and 10.96% for the RT-2 M-16 h and PEO coatings, respectively, in terms of Ti 2p XPS spectra.

According to Fig. 7(a) and Fig. S5, although the removal of OH functional groups (RTO-2 M-16 h coating) caused a decrease of 0.33 times in the degradation rate constant compared to the RT-2 M-16 h coating, the degradation rate constant of the RTO-2 M-16 h increases by 2.27 times compared to the PEO coating, proving the direct effect of OVs on PA.

From Fig. 7(b) and (c) and Table 2, it is evident that the contribution of the hydroxyl groups in the RTO-2 M-16 h is lower than that of the RT-2 M-16 h, while the contribution of oxygen vacancy is equal in both

coatings. Therefore, a relative removal of the surface hydroxyl groups in the RTO-2 M-16 h could detrimentally affect photocatalytic efficiency. To be more specific, hydroxyl groups, especially the isolated ones, function as adsorption sites for organic pollutants through the OH···π-electron-type interaction. Additionally, the hydroxyl groups possess the ability to capture the photoinduced holes to generate strong oxidizing agents such as HO[•], which attack adsorbed species in synergy with other radicals such as O₂^{•-} to proceed with degradation [91].

3.5. Condition-dependence and photocatalytic stability of optimal post-alkali-treated PEO coating

The variation trends of TC photo-degradation over the RT-2 M-16 h coating at different initial concentrations are shown in Fig. 8(a). According to Fig. 8(a), the degradation efficiency was significantly reduced with the increment in the primary TC concentration from 5 to 20 mg·L⁻¹ [92–94]. This behavior could be ascribed to the reduction of active sites on the photo-catalyst and absorption of more light due to the adsorption of TC molecules; both factors cause fewer photons to arrive at the surface of the catalyst. Additionally, increasing the initial concentration of TC could produce more organic intermediates and end-products, which would compete with the parent molecules of TC for the otherwise same number of photocatalytic sites and thus, inhibit the TC photocatalytic degradation [95–97].

To assess the success and effectiveness of the photo-catalyst in TC photo-degradation, the PCE values of the prepared coatings and the only available hydrothermal coating (calculated by Eq. 5, [98]), as well as the FoM values of photocatalytic powders (calculated by Eq. 6, [99]), were summarized in Table S3.

$$PCE = \frac{\text{conversion efficiency}(\%) \times \text{initial pollutant concentration(ppm)}}{\text{catalyst area(cm}^2\text{)} \times \text{irradiation time(min)} \times \text{light source power(W)}} \quad (5)$$

Among different coatings, the highest PCE upon visible irradiation was allocated to the RT-2 M-16 h coating, which can be ascribed to the role of the optimal amount of oxygen vacancy in PA improvement. Moreover, it is seen that the values of PCE are higher than that of FoM for visible light TC photo-degradation mediated by photocatalytic powders, which can be originated from different contributing factors such as reactor geometry and the presence of “initial pollutant concentration” in the denominator of the fraction in the FoM equation. We also advise caution in the direct comparison of powdered photo-catalysts with coatings.

The pH plays a significant role in photocatalytic activity by modifying the adsorption properties and the availability of HO[•] [97]. In fact, the pH modifies both the TC chemical structure in the solution and the surface properties of the photocatalyst. As seen in Fig. 8(b), based on the pH drift method (Supplementary Text S1), the pH_{pzc} value of the RT-2 M-16 h coating was estimated to be around 6.3. As typically approved, for pH < pH_{pzc} and pH > pH_{pzc}, the surface of the coating is positively and negatively charged, respectively [97,100,101]. TC is an amphoteric molecule having multiple functional groups ionizable; thus, depending on the pH of the solution, the general charge of TC can be positive (TC⁺, pH < pK_{a1} = 3.3), neutral (TC⁰, pK_{a1} = 3.3 < pH < pK_{a2} = 7.68), or negative (TC⁻, pH > pK_{a2} = 7.68) [102,103]. Indeed, as shown in Fig. 8(c), according to the repulsive force between the TC⁺ and the positively charged on the RT-2 M-16 h surface at pH 3, the

photo-degradation of TC was decreased [74]. Moreover, with an increasing amount of Cl^- ion by the HCl agent, which is responsible for acidifying the TC solution, the consumption of photogenerated holes by inhibiting the generation of HO^\bullet causes a further decrease in PA [104]. The photodegradation of TC improved with increasing pH values relative to acidic pH. As the pH of the solution increased, the hydroxide anions produced more HO^\bullet from the oxidation of holes in the photocatalytic system (to be validated with DRS and Mott-Schottky), which should be the major reason for improving the PA of alkaline pH compared to acidic pH [105]. In addition, owing to the repulsive force between the anionic form of the TC molecule and the negatively charged surface of the coating at alkaline pH (pH=9) [74], the TC degradation rate is lower than that of neutral pH. Therefore, at alkaline pH, the effect of repulsive interaction overcomes the effect of HO^\bullet formation, which reduces the PA at pH= 9. Consequently, the TC solution at pH of 7.2 is optimal for the best photocatalytic activity.

According to Fig. 8(d), the stability of the RT-2 M-16 h coating for TC photo-degradation upon visible light irradiation was examined by the recycling test. Results show a slight reduction in the photocatalytic efficiency of the RT-2 M-16 h in the second run compared to the first run, which had 78% degradation under the same conditions. The residual catalytic products and the absorbed organic compounds on the photo-catalysts' surface are inclined to turn the hydrophilic surface into a hydrophobic one, leading to a decline in the photo-degradation rate after use. After the second run, no apparent deactivation/passivation of the photo-catalyst was observed, indicating the excellent stability of the RT-2 M-16 h for TC photo-degradation under visible light. So, photocatalysis can decompose the organic compounds on the surface, restoring hydrophilicity, in turn, maintaining the photocatalytic activity after 5 runs [106]. Therefore, this photo-catalyst can be sustainable and reusable to scale up for industrial applications.

Moreover, the photo-degradation efficiency of the TC via the RT-2 M-16 h coating under visible light illumination for a different storage time of the RT-2 M-16 h is presented in Fig. 8(e). No meaningful change was seen, which can be attributed to the consistent levels of OVs and the reliable stability of photo-catalysts for long-term application.

3.6. Photocatalytic mechanism of TC photodegradation over post-alkali-treated PEO coating

To compare the light absorption of the PEO and RT-2 M-16 h coatings, the UV-Vis diffuse reflectance spectra (DRS) analysis was performed, as shown in the inset of Fig. 9(a). The RT-2 M-16 h coating presented an obvious light absorption, which was much larger than the PEO coating. This strong absorption is ascribed to the presence of OVs (Ti^{3+}), which induce a continuous vacancy band of electronic states under the CB edge of the RT-2 M-16 h coating [107,108]. Also, the higher light absorption of the RT-2 M-16 h coating is in good agreement with the color transformation of plain PEO coating (Fig. 4(c)).

Moreover, the UV-Vis DRS was utilized to gather further insights into the photocatalytic degradation mechanism as well as the determination of the coating band gap [109]. According to the absorption spectra, the relative optical band gap value of the PEO and RT-2 M-16 h coatings was determined using the Tauc equation (Eq. 7) [64]:

$$\alpha h\nu = B(h\nu - E_g)^n \quad (7)$$

Where h is Planck's constant, α is the absorption coefficient, ν is light frequency, and B is a constant. $n = 2$ is a constant for the indirect electronic transition mode of the TiO_2 semiconductor [64,110]. To compute the values of the band gap in the coatings, extrapolating the linear zone of $[\alpha h\nu]^{0.5}$ vs. $h\nu$ plot to the intersection with the $h\nu$ -axis (Fig. 9(a)) was used [63]. The band gaps of the PEO and RT-2 M-16 h coatings for the indirect transition were 3.01 and 2.60 eV, respectively. Since the band gap of the PEO coating containing 89.89% of the anatase phase

(3.2 eV) and 10.11% of the rutile phase (3.0 eV) was estimated to be 3.01 eV, it seems that the band gap narrowing stemmed from the existence of Na and P elements [111–113], as confirmed in the EDS results. In addition, the difference in the percentage of Na and P elements in the PEO and RT-2 M-16 h coatings was negligible, so the band gap reduction in the RT-2 M-16 h coating could be originating from other factors, which will be later assessed on. The narrowed band gap for the RT-2 M-16 h coating can be attributed to the overlap of vacancy-induced mid-gap states with the CB by NaOH post-alkali treatment on the PEO coating, which results in the down-shift of the CB minimum [49,68,77,114,115]. The more powerful absorption in the feasible light zone helps the use of solar light, giving an increase to more photo-generated holes and electrons for later photocatalytic reactions [116].

The VB and CB edge positions of the PEO and RT-2 M-16 h are pivotal to assessing the involved ROS in the photocatalytic mechanism [117,118]. Due to the uncertainty of the electronegativity (χ) determination for TiO_2 -containing OVs based on the Mulliken formula [119], the Mott-Schottky analysis was used in appraising the evaluation of semiconductor materials type and flat band potential (E_{FB}) [120–122]. The Mott-Schottky plots for the PEO and optimal post-alkali-treated PEO coatings are shown in Fig. 9(b). The n-type semiconductor behavior of both coatings stemmed from the graphs' positive slope. From the intercept of the tangent of the Mott-Schottky plot on the x-axis, the V_{fb} for the PEO and RT-2 M-16 h coatings was estimated to be about -0.86 V and -0.3 V vs. Ag/AgCl, corresponding to -0.35 and $+0.225$ V vs. NHE (from Eq. 8 [121]), respectively. It is reported that the flat band potential is close to the CB position of an n-type semiconductor [120]. So, E_{CB} for the RT-2 M-16 h was estimated to be $+0.225$ V vs. NHE.

$$(E_{CB} = E_{NHE}) = (E_{(Ag/AgCl)} = V_{fb}) + 0.197 + 0.059 \times (pH_{NaCl} = 5.57) \quad (8)$$

Considering the band gap of RT-2 M-16 h (2.6 eV), the E_{VB} of the RT-2 M-16 h can be determined to be 2.825 V vs. NHE.

Moreover, the electron transmission performance of the catalysts can be evaluated via Mott-Schottky analysis. From Fig. 9(b), the RT-2 M-16 h coating gave a flat slope compared with the PEO coating, indicating increased transport of electrons. The existence of OVs and Ti^{3+} as donor states below the CB of RT-2 M-16 h leads to a redistribution of additional electrons between OV sites and the nearest neighboring atoms of Ti to attain charge equilibrium, which in turn, increases the charge carrier density and electrical conductivity of the RT-2 M-16 h coating [123].

Scavenging tests were also performed to understand the photocatalytic mechanism and qualitatively assess the radicals generated during the TC photo-degradation over the optimal post-alkali-treated PEO coating under visible light illumination [124]. Isopropanol (C_3H_8O), Chloroform ($CHCl_3$), sodium azide (NaN_3), EDTA-2Na ($C_{10}H_{14}N_2Na_2O_8$), and sodium pyruvate ($C_3H_3NaO_3$) were respectively exploited to quench hydroxyl radicals ($HO^\bullet = 2 \times 10^9 M^{-1}s^{-1}$), hydroxyl and superoxide radical ($HO^\bullet = 5.4 \times 10^7 M^{-1}s^{-1}$ and $O_2^\bullet = 3 \times 10^{10} M^{-1}s^{-1}$), hydroxyl radical and singlet oxygen ($HO^\bullet = 1.2 \times 10^{10} M^{-1}s^{-1}$ and $^1O_2 = 3 \times 10^{10} M^{-1}s^{-1}$), hole (h^+) and H_2O_2 [125–127]. Here, to accurately evaluate the relative contributions of the as-mentioned radicals to the compound degradation, scavenging capacity (SC) should be calculated using the amount of ck (c and k are the concentration and the reaction rate constant of the scavengers). To obtain the real effect of 1O_2 , the SC of isopropanol and NaN_3 for HO^\bullet should be initially matched, and then the difference between isopropanol and NaN_3 on TC degradation reflects the contribution of 1O_2 . The SC for HO^\bullet of isopropanol at 1 mM was calculated to be $2.3 \times 10^6 s^{-1}$ and for HO^\bullet and 1O_2 of NaN_3 at 0.1 mM were equal to $1.2 \times 10^6 s^{-1}$ and $2 \times 10^5 s^{-1}$, respectively. Furthermore, as shown in Fig. 9(c), in the presence of isopropanol and NaN_3 , the percentage of TC

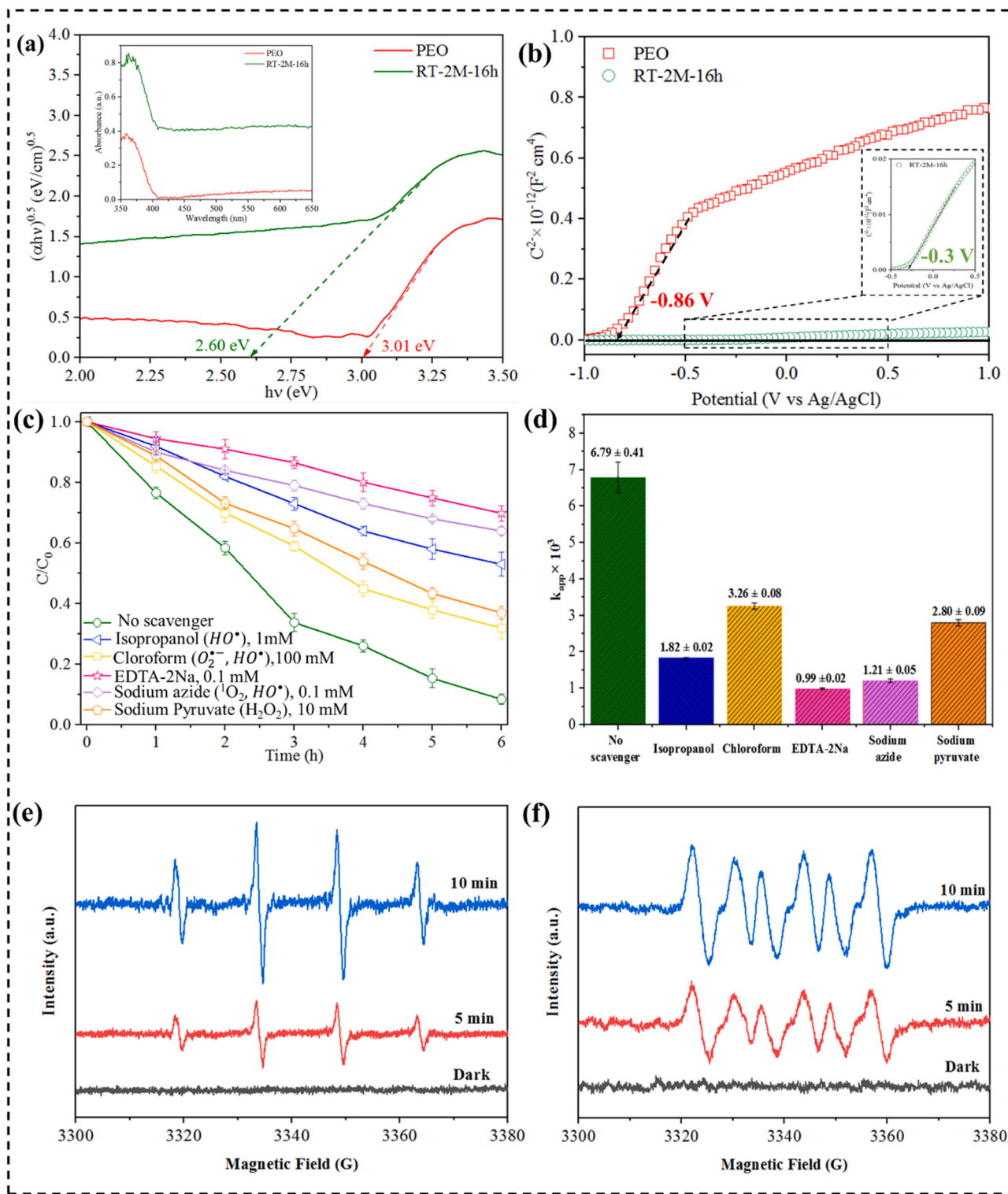


Fig. 9. (a) Tauc Plots obtained from the DRS analysis of the $(\alpha h\nu)^{0.5}$ vs. $h\nu$ plots of the PEO and RT-2 M-16 h coatings, inset depicts the UV-visible diffuse reflectance spectra of the PEO and RT-2 M-16 h coatings (b) Mott-Schottky plots of the PEO and RT-2 M-16 h coatings at a frequency of 1000 Hz in 3.5 wt% NaCl aqueous solution, (c) Effect of scavengers on the photocatalytic degradation of TC, (d) values of reaction rate constants mediated by the RT-2 M-16 h under visible light for Isopropanol (1 mM), Chloroform (100 mM), EDTA-2Na (0.1 mM) and Sodium azide (0.1 mM). Experimental conditions: $[\text{TC}]_0 = 15 \text{ mg.L}^{-1}$, light intensity = 540 mW/cm², pH = 7.2. ESR signal of DMPO-HO[·] (e) and DMPO-O₂^{·-} (f) adducts over the RT-2 M-16 h coating.

degradation plummeted from 91.52% to 47% and 36%, respectively. The difference between decreasing the TC degradation percentage for isopropanol and NaN₃ can be attributed to the effect of ${}^1\text{O}_2$.

In contrast, based on the SC value, chloroform at 100 mM is capable of quenching anion superoxide ($3 \times 10^9 \text{ s}^{-1}$) at a rate that is 1000 times

higher than that of hydroxyl radical ($5.4 \times 10^6 \text{ s}^{-1}$). So, when Chloroform was added, the percentage of TC degradation decreased from 91.52% to 68%. Moreover, after the addition of EDTA-2Na, a remarkable loss of photocatalytic activity could be observed, revealing that photo-generated holes play a significant role in the photo-degradation of

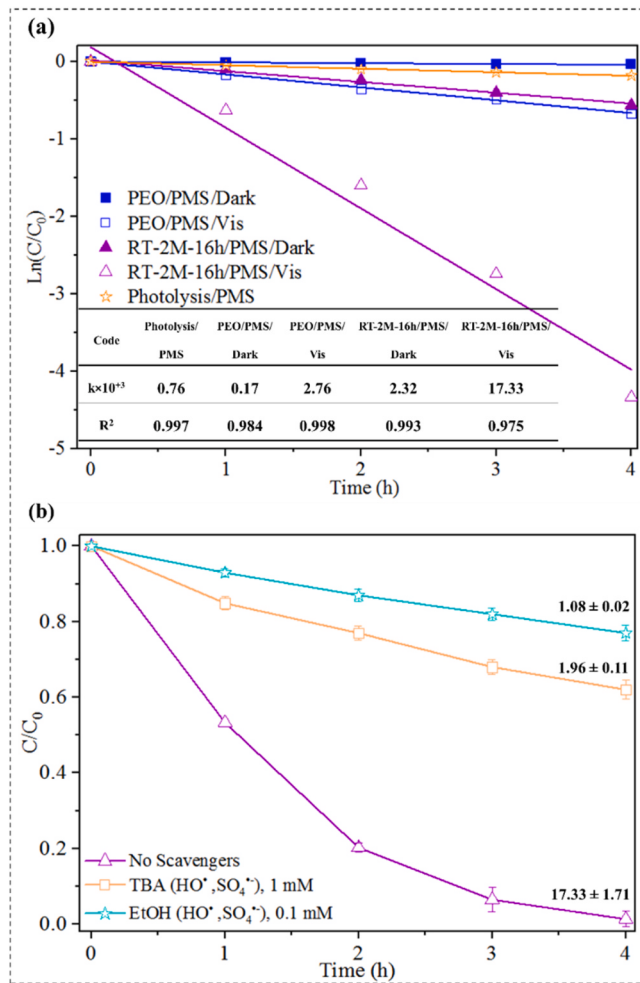


Fig. 10. (a) Reaction kinetics of TC degradation with the PEO and RT-2 M-16 h coatings in the presence of PMS under dark and solar light irradiation conditions (b) Effect of TBA (1 mM) and EtOH (0.1 mM) on TC degradation in the RT-2 M-16 h/PMS system, Experiment conditions: $[\text{TC}]_0 = 15 \text{ mg.L}^{-1}$; $[\text{PMS}]_0 = 0.5 \text{ mM}$.

Table 3
The synergistic factors for PMS activation by the RT-2 M-16 h and plain PEO coating under visible illumination.

Experiment	Conditions	$k_{\text{app}} \times 10^3$ (min ⁻¹)	Synergistic Factor
1	Photolysis (TC/Vis)	0.57 ± 0.02	-
2	Photolysis/PMS (TC/PMS/Vis)	0.75 ± 0.02	
3	PMS (TC/PMS/Dark)	0.04 ± 0.005	
4	Adsorption (PEO/TC/Dark)	0.07 ± 0.006	PEO = 1.40
5	Coating/Vis (PEO/TC/Vis)	1.74 ± 0.32	
6	Coating/PMS/Dark (PEO/TC/ PMS/Dark)	0.16 ± 0.01	
7	Coating/PMS/Vis PEO/TC/PMS/Vis	2.76 ± 0.05	
8	Adsorption (RT-2 M-16 h/TC/Dark)	0.06 ± 0.009	RT-2 M-16 h = 2.10
9	Coating/Vis (RT-2 M-16 h/TC/Vis)	5.84 ± 0.46	
10	Coating/PMS/Dark (RT-2 M-16 h/TC/PMS/Dark)	2.32 ± 0.09	
11	Coating/PMS/Vis (RT-2 M-16 h/TC/PMS/Vis)	17.33 ± 1.39	

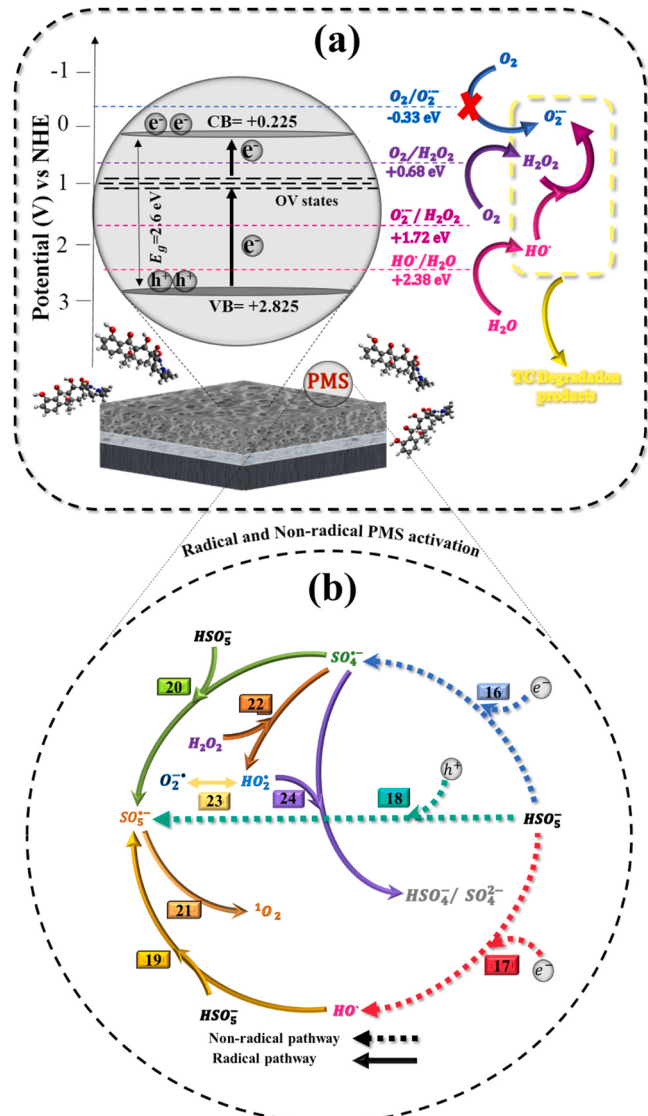


Fig. 11. The proposed photocatalytic mechanism of the post-alkali-treated PEO coating under visible-light irradiation (a) without and (b) with PMS.

TC, as reported elsewhere [128]. Indeed, by adding EDTA-2Na, not only holes can directly degrade TC but also inhibit the formation of hydroxyl radicals. With the addition of sodium pyruvate, the photo-degradation of TC decreased from 91.52% to 62.9%. It is suggested that H_2O_2 does not directly interact with the target reactant in the degradation of TC, but generates O_2^\cdot through Eq. (13), which reacted with the target TC molecules [127]. Therefore, according to the results of related rate constants for TC degradation mediated by different scavengers in Fig. 9 (d), the importance of active species in TC photo-degradation can be ranked as follows: ${}^1\text{O}_2 < \text{O}_2^\cdot < \text{HO}^\cdot < \text{h}^+$. The direct proofs of HO^\cdot and O_2^\cdot generation on the RT-2 M-16 h coating was achieved by ESR method, illustrated in Fig. 9(e) and (f). Neither DMPO- HO^\cdot nor O_2^\cdot characteristic signals were detected under dark conditions. While the existence of the four-line 1:2:2:1 ESR spectrum in Fig. 9(e), can be attributed to DMPO- HO^\cdot spin adducts, obviously confirming the ability of the RT-2 M-16 h coating to produce hydroxyl radicals upon visible light irradiation. As can be seen in Fig. 9(f), the obtained complex ESR spectrum ascribed to DMPO- O_2^\cdot signal was also attained. It is worth mentioning that irradiation time prolonging to 10 min corroborates the development of O_2^\cdot and HO^\cdot mediated by the RT-2 M-16 h coating under visible light illumination.

TOC analysis was performed to study the TC mineralization efficiency on the RT-2 M-16 h coating (Fig. S6). After 6 h of treatment, the TC degradation efficiency of RT-2 M-16 h was about 91.52%, while only 53.05% of TOC removal was observed. This result indicated that although TC was degraded, it was not completely mineralized [74,129, 130].

Additionally, the efficiency of the chemical oxidation of the organic carbon during photocatalysis can be computed using the average oxidation state of carbon (AOS) = 4 (1-(COD/TOC)), where TOC and COD denote total organic carbon (mol C.L⁻¹) and chemical oxygen demand (mol O₂. L⁻¹) [131,132]. Accordingly, AOS varies between + 4 and - 4 for the most oxidized (CO₂) and reduced (CH₄) state of carbon, respectively. The results demonstrate that during TC photo-degradation, the value of AOS was increased from - 0.43 (initial value) to + 2.02 after 6 h illumination (approaching + 4), indicating a significant reduction in COD in the photo-degradation of the treated TC solution,

$$S_{Coating/PMS/Vis} = \frac{k_{Coating/PMS/Vis}}{k_{Photolysis} + k_{PMS} + k_{adsorption} + (k_{Photolysis/PMS} - k_{Photolysis} - k_{PMS}) + (k_{Coating/Vis} - k_{adsorption} - k_{Photolysis}) + (k_{Coating/PMS} - k_{PMS} - k_{adsorption})} \quad (15)$$

and the TOC reduction in conjunction with the COD results indicates its mineralization, i.e., conversion to CO₂.

Based on the scavenging results and the results of the DRS and Mott-Schottky, the mechanism of TC photodegradation reaction was proposed using the optimal post-alkali-treated PEO coating and schematically illustrated in Fig. 11(a). Under visible light irradiation, due to the OV introduction on the surface of the RT-2 M-16 h, the electrons can be excited from the VB to the CB and OV states, leaving holes with oxidative potential in the VB. The photo-excited holes in the VB of the RT-2 M-16 h play two key roles: the first is facilitating the direct oxidation of TC (as confirmed by the scavenging test, Fig. 9(c)) and the second role, the generation of the HO• radical due to the VB potential being sufficiently more positive than the potential of HO•/OH and HO•/H₂O, suggesting that the holes could react with water molecules and hydroxyl groups according to Eqs. 9 and 10 [87].



Also, based on Eq. 11 [133] ($E^0: 0.68$ V vs. NHE, $k = 5.5 \times 10^9$ M⁻¹s⁻¹) H₂O₂ can be generated via the termination reaction of HO• radical recombination.



The excited electrons on the CB and OV states of the RT-2 M-16 h cannot directly reduce dissolved oxygen in the reaction solution to generate O₂^{•-}, owing to the more positive value of E_{CB} than the standard redox potential of O₂/O₂^{•-} = -0.33 (Eq. 12). Since the presence of O₂^{•-} was confirmed by the scavenging test (Fig. 9(c)) and ESR analysis (Fig. 9(f)), the alternative reaction based on Eq. 13 ($E^0: 1.72$ V vs. NHE) was proposed for O₂^{•-} generation [133,134]. Moreover, in the presence of superoxide and strongly oxidative holes, the formation of ¹O₂ cannot be excluded (Eq. 14), given that isopropanol does not fully block TC degradation and the remainder is higher than the photolysis rate.



3.7. PMS-accelerated photocatalytic efficiency of the PEO and optimal coatings for TC degradation: perspectives and integrated mechanism

The impact of PMS activation mediated by the PEO and optimal post-alkali-treated PEO coatings on the degradation rate constant of TC degradation in dark and visible conditions were compared (Fig. 10(a) and Fig. S7). The system of PEO/PMS displayed an exceptionally low activity of TC under both circumstances that has $k = 0.16 \times 10^{-3}$ min⁻¹ in the dark vs $k = 2.76 \times 10^{-3}$ min⁻¹ under visible light as they are weak PMS activators. Nevertheless, the system of RT-2 M-16 h/PMS exhibited accelerated TC removal that has $k = 2.32 \times 10^{-3}$ min⁻¹ in the dark, and enhanced activity of oxidation, at $k = 17.33 \times 10^{-3}$ min⁻¹ under visible light. So, the RT-2 M-16 h/PMS/Vis system is 6.27 times more photoactive than the PEO/PMS/Vis system. An assessment of the synergistic effects of the constituents of the net process is made via the rate constants, as follows (Eq. 15) [135]:

Table 3 displays the synergistic factor for the activation of PMS and the constant rates using the PEO and RT-2 M-16 h coatings. The synergistic factor of PEO/PMS/Vis and RT-2 M-16 h/PMS/Vis systems was estimated to be 1.40 and 2.10, respectively. One can see that the use of the RT-2 M-16 h catalysts is highly beneficial in PMS-enhanced TC degradation. These results were attributed to the fact that the RT-2 M-16 h coating with a significant number of OVs serves as a catalyst and photocatalyst for activation of PMS [8] and possesses better characteristics, such as high absorption of visible light (see Fig. 9(a)) and decent mobility of electrons (see Fig. 9(b)), leading to the accelerated TC degradation.

To study the principal photo-produced reactive intermediates produced within the enhanced photocatalytic degradation of TC in the RT-2 M-16 h/PMS/Vis system, quenching experiments were performed by adding various radical scavengers. Although EtOH could easily react with both HO• ($1.2\text{--}2.8 \times 10^9$ M⁻¹ s⁻¹) and SO₄^{•-} ($1.6\text{--}7.7 \times 10^7$ M⁻¹ s⁻¹), TBA has a much superior rate constant with HO• ($3.8\text{--}7.6 \times 10^8$ M⁻¹ s⁻¹) in comparison to SO₄^{•-} ($4.0\text{--}9.1 \times 10^5$ M⁻¹ s⁻¹) [136,137]. So, TBA reacts with HO• 1000 times quicker comparing with SO₄^{•-}, as such, the mixture of these experiments can isolate the role of HO• in this reaction [119]. Also, to obtain the effect of SO₄^{•-}, we need to match the SC value of EtOH and TBA for HO•. The SC value for HO• and SO₄^{•-} of TBA at 1 mM was calculated to be 6×10^5 s⁻¹ and 4×10^2 s⁻¹, respectively and the scavenging capacities for HO• and SO₄^{•-} of EtOH at 0.1 mM were calculated to be 1.9×10^5 and 3.5×10^3 s⁻¹, respectively. As shown in Fig. 10(b), after adding TBA into the solution, TC removal efficiency dropped to 38%. Also, with the addition of EtOH, TC removal efficiency plunged to 23%, confirming the generation of SO₄^{•-} and HO• radicals and the dominant role of HO• radical in TC degradation process and the difference in inhibition behavior is due to more scavenging of sulfate radical by EtOH.

As shown in Fig. 11(b), the presence of PMS as an oxidant resulted in the generation of further reactive species participating in the photocatalytic mechanism as follows: The degradation mechanism with PMS in the reaction system was divided into radical and non-radical species [138]. The photogenerated electron-hole under light irradiation can non-radically activate PMS and generate radicals, such as SO₄^{•-}, HO•, and SO₅^{•-} (Eq. 16-18).



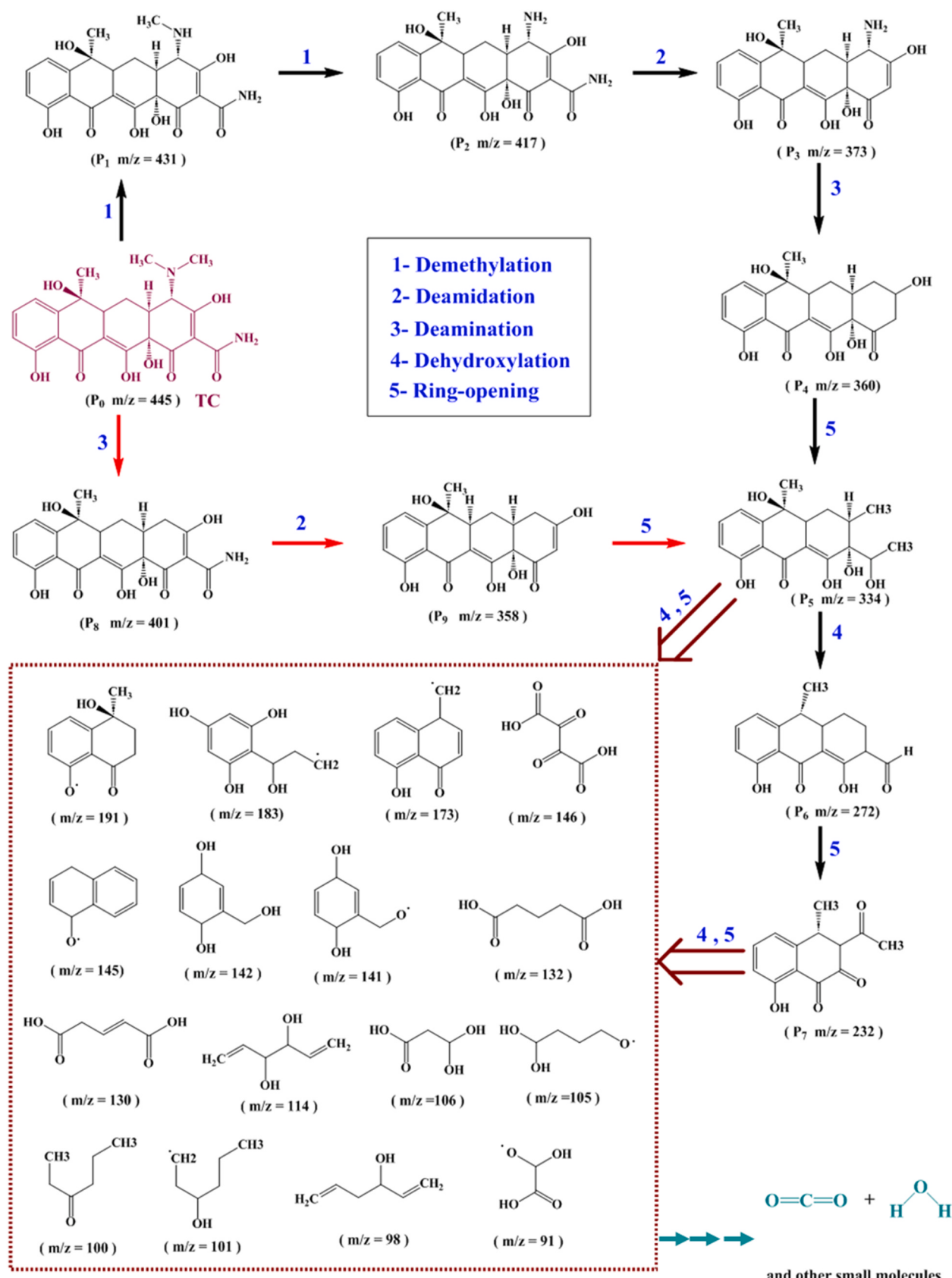


Fig. 12. Possible pathways for TC degradation in the RT-2 M-16 h/PMS/Vis system. The small molecules after 6 h TC photodegradation are illustrated in the dashed box.

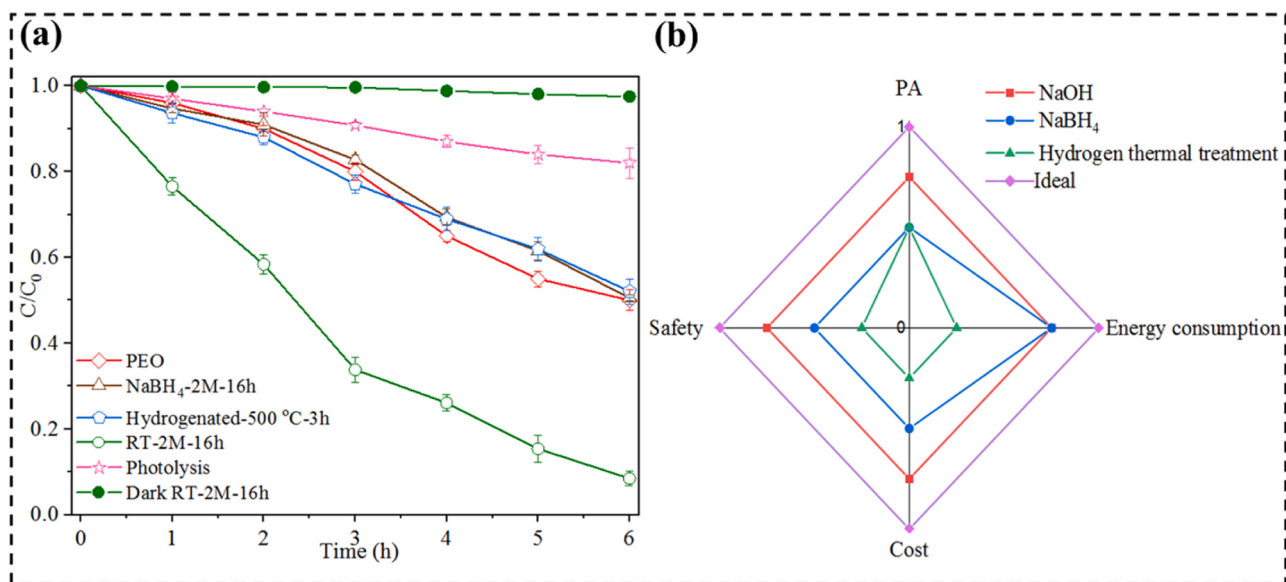
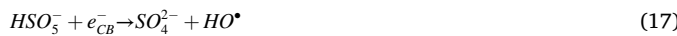
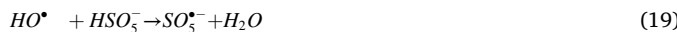


Fig. 13. (a) Evaluating the photocatalytic activity of produced coatings with various approaches of OV formation on the PEO coating, (b) Comparative assessment of different methods for introducing OVs on the surface of the PEO coating.



Based on a radical pathway, the as-formed radicals can lead to the generation of \$\text{SO}_5^\bullet\$ according to Eqs. 19 and 20 [133]. The recombination of \$\text{SO}_5^\bullet\$ radicals readily proceeded due to the high reaction rate (\$k = 2 \times 10^8 \text{ M}^{-1} \text{ s}^{-1}\$) and low activation energy (\$E = 7.4 \pm 2.4 \text{ kcal mol}^{-1}\$), resulting in the fast generation of \${}^1\text{O}_2\$ (Eq. 21) [139].



Since the formation of \$\text{H}_2\text{O}_2\$ species during TC photodegradation was confirmed in Eq. 11, considering that the pH of the solution after PMS addition was changed to 4.81, \$\text{H}_2\text{O}_2\$ subsequently reacted with \$\text{SO}_4^{2-}\$ to form \$\text{HO}_2^\bullet\$ (Eq. 22), causing the other propagation reactions (Eqs. 23 and 24) [133,140].



Moreover, the possible intermediate products of TC degradation in the RT-2 M-16 h/PMS/Vis system were identified by LC-MS techniques, and based on the results, two possible degradation pathways were proposed (Fig. 12). In both pathways, photodegradation of TC might begin by \$\text{HO}^\bullet/\text{SO}_4^{2-}\$ and \$h^+\$. According to the test results, the main detected intermediate products were the \$P_1(m/z = 431)\$, \$P_2(m/z = 417)\$, \$P_3(m/z = 373)\$, \$P_4(m/z = 360)\$, \$P_5(m/z = 334)\$, \$P_6(m/z = 272)\$, \$P_7(m/z = 232)\$ and \$P_8(m/z = 401)\$, \$P_9(m/z = 358)\$ (Appendix a Table S4) [141,142]. Also, final fragments with \$m/z = 91\$, 100, 101, 105, 132, 141, 142, 145, 173, and 183 have high abundance percentages. According to some existing literature [143,144], the proposed possible pathways for TC photodegradation involve a combination of

de-methylation, de-hydroxylation, ring-opening, deamination, and deamidation in the RT-2 M-16 h/PMS/Vis system.

3.8. Comparison of the optimal coating with different methods of introducing OVs

As mentioned in the introduction section, to compare different methods for introducing surface OVs on the PEO coating, two common methods were assessed as follows: hydrogen thermal treatment of the PEO was carried out in a tube furnace with a hydrogen flow of \$100 \text{ mL min}^{-1}\$ for 3 h at \$500^\circ\text{C}\$ [33] and chemical reduction via \$\text{NaBH}_4\$ (2 M, 16 h) as a reducing agent. To sum up, a novel point of this work is the comparison of various approaches of OV formation on the coating, assessed by evaluating the photocatalytic activity of produced coatings in organic contaminants other than dyes; according to Fig. 13(a), the employment of \$\text{NaOH}\$ as a reducing agent was chosen as the optimal approach.

To compare the conventional methods for introducing OVs on \$\text{TiO}_2\$, the energy consumption (during treatment), cost, safety, and photocatalytic efficiency were normalized and ranked on a 0–1 scale, illustrated in Fig. 13(b). The minimum and maximum performance of the method are assigned values of 0 and 1, respectively. As a result, the outer shell is indicative of the ideal condition.

Due to annealing at elevated temperatures under a hydrogen atmosphere, the energy consumption of hydrogenated \$\text{TiO}_2\$ coating is more than the post-alkali-treatment with different reducing agents at room temperature. To evaluate the safety of the post-alkali treatment at room temperature, average values of the hazardous materials identification system (HMIS) of the reducing agents including the reactivity, health hazard, and fire hazard were considered. Therefore, the use of \$\text{NaOH}\$ as a reducing agent is safer than \$\text{NaBH}_4\$. Also, it is universally accepted that the minimum level of safety is related to the risk of explosion in the hydrogen thermal treatment. Moreover, the cost of energy and \$\text{H}_2\$ consumption, hydrogen thermal treatment cost is much more than the other methods. The photocatalytic degradation of tetracycline of different coatings was assessed based on Fig. 13(a). To sum up, the larger surface area corresponds to the chemical reduction using \$\text{NaOH}\$ as a reducing agent, resulting in the best performance. So,

post-alkali-treated PEO coating using NaOH seems the most effective method to prepare coatings suitable for photocatalytic applications.

4. Conclusions

A series of photo-catalytic TiO₂ coatings with varying oxygen vacancy concentrations were prepared using the PEO process and NaOH post-alkali treatment to investigate their photocatalytic efficiency in TC photodegradation. Microstructural analysis revealed typical PEO coating surfaces with abundant pores of diverse sizes uniformly distributed. Phase analysis showed that room temperature post-alkali treatment did not affect the crystalline phases' percentage, contributing to the material's enhanced photocatalytic performance.

Photocatalytic experiments demonstrated that TC decomposition under visible light irradiation can be significantly enhanced (x3.41 times in our study) by increasing NaOH concentration during alkaline treatment. The optimized post-alkali-treated PEO coating exhibited improved separation efficiency of photogenerated charge carriers due to the PEO treatment induced surface defects. The coating's narrower band gap and stronger visible light absorption were attributed to the overlap of vacancy-induced mid-gap states and the CB, resulting in the down-shift of the CB edge minimum.

Additionally, the optimal coating showed remarkable proficiency in activating PMS, efficiently degrading TC even under visible light. Besides, LC-MS analysis detected various intermediate products, proving a high degree of mineralization and supporting the proposed experimental pathway when combined with radical scavenger and EPR tests.

Considering these enhancements from NaOH post-treatment, this low-cost process offers exciting potential for water treatment applications, making the material an attractive choice.

CRediT authorship contribution statement

Reza Hosseini: Investigation, Visualization, Writing – review & editing, **Arash Fattah-alhosseini:** Supervision, Conceptualization, Methodology, Validation, Resources, Writing – review & editing, Funding acquisition, **Minoo Karbasi:** Conceptualization, Methodology, Visualization, Investigation, Validation, Writing – review & editing, **Stefanos Giannakis:** Conceptualization, Methodology, Validation, Visualization, Writing – review & editing.

Declaration of Competing Interest

The authors declare that they have no known competing financial interests or personal relationships that could have appeared to influence the work reported in this paper.

Data Availability

Data will be made available on request.

Acknowledgments

The financial support of Bu-Ali Sina University for this research is appreciated. Stefanos Giannakis acknowledges the ARPHILAKE project, "Combating Antibiotic Resistance in Philippine Lakes: One Health upstream interventions to reduce the burden", which received funding from the Agencia Estatal de Investigación (Spain), Proyectos de Colaboración Internacional (PCI2022-132918), under the umbrella of the "JPIAMR - Joint Programming Initiative on Antimicrobial Resistance". Stefanos Giannakis would also like to acknowledge the DETRAS Project, "Desinfección-Descontaminación de Efluentes Contra la Transmisión de la Resistencia en Antibióticos" (APOYO-JOVENES-21-UXUKHL-88-WQWWQF), funded by the Comunidad de Madrid through the call "Research Grants for Young Investigators from Universidad Politécnica de Madrid".

Appendix A. Supporting information

Supplementary data associated with this article can be found in the online version at doi:10.1016/j.apcatb.2023.123197.

References

- [1] Y. Zhang, C. Liu, B. Xu, F. Qi, W. Chu, Degradation of benzotriazole by a novel Fenton-like reaction with mesoporous Cu/MnO₂: Combination of adsorption and catalysis oxidation, Appl. Catal. B Environ. 199 (2016) 447–457, <https://doi.org/10.1016/j.apcatb.2016.06.003>.
- [2] S. Giannakis, S. Samoilis, J. Rodríguez-Chueca, A meta-analysis of the scientific literature on (photo)Fenton and persulfate advanced oxidation processes: where do we stand and where are we heading to? Curr. Opin. Green. Sustain. Chem. 29 (2021), 100456 <https://doi.org/10.1016/j.cogsc.2021.100456>.
- [3] P. Hu, M. Long, Cobalt-catalyzed sulfate radical-based advanced oxidation: a review on heterogeneous catalysts and applications, Appl. Catal. B Environ. 181 (2016) 103–117, <https://doi.org/10.1016/j.apcatb.2015.07.024>.
- [4] M. Kohantobari, G. Moussavi, S. Giannakis, A review of the innovations in metal- and carbon-based catalysts explored for heterogeneous peroxyomonosulfate (PMS) activation, with focus on radical vs. non-radical degradation pathways of organic contaminants, Chem. Eng. J. 411 (2021), 127957, <https://doi.org/10.1016/j.cej.2020.127957>.
- [5] C. Wang, J. Kim, V. Malgras, J. Na, J. Lin, J. You, M. Zhang, J. Li, Y. Yamauchi, Water purification: metal-organic frameworks and their derived materials: emerging catalysts for a sulfate radicals-based advanced oxidation process in water purification (Small 16/2019), Small 15 (2019) 1970085, <https://doi.org/10.1002/smll.201970085>.
- [6] Z. Wang, Y. Chen, P. Xie, R. Shang, J. Ma, Removal of *Microcystis aeruginosa* by UV-activated persulfate: Performance and characteristics, Chem. Eng. J. 300 (2016) 245–253, <https://doi.org/10.1016/j.cej.2016.04.125>.
- [7] S. Giannakis, K.Y.A. Lin, F. Ghanbari, A review of the recent advances on the treatment of industrial wastewaters by Sulfate Radical-based Advanced Oxidation Processes (SR-AOPs), Chem. Eng. J. 406 (2021), 127083, <https://doi.org/10.1016/j.cej.2020.127083>.
- [8] H.Y. Yoo, M.S. Kim, H. Shin, J. Lim, Peroxymonosulfate activation by black TiO₂ nanotube arrays under solar light: Switching the activation mechanism and enhancing catalytic activity and stability, J. Hazard. Mater. 433 (2022), 128796, <https://doi.org/10.1016/j.jhazmat.2022.128796>.
- [9] M.B. Tahir, T. Iqbal, M. Rafique, M.S. Rafique, T. Nawaz, M. Sagir, Nanomaterials for photocatalysis, in: Nanotechnol. Photocatal. Environ. Appl., Elsevier, 2020, pp. 65–76, <https://doi.org/10.1016/B978-0-12-821192-2.00005-x>.
- [10] J. Moma, J. Baloyi, Modified titanium dioxide for photocatalytic applications, Photocatal.- Appl. Attrib., IntechOpen (2019), <https://doi.org/10.5772/intechopen.79374>.
- [11] M.S.S. Danish, L.L. Estrella, I.M.A. Alemaida, A. Lisin, N. Moiseev, M. Ahmadi, M. Nazari, M. Wali, H. Zaheb, T. Senju, Photocatalytic applications of metal oxides for sustainable environmental remediation, Metals 11 (2021) 1–25, <https://doi.org/10.3390/met11010080>.
- [12] X. Xiang, L. Wu, J. Zhu, J. Li, X. Liao, H. Huang, J. Fan, K. Lv, Photocatalytic degradation of sulfadiazine in suspensions of TiO₂ nanosheets with exposed (001) facets, Chin. Chem. Lett. 32 (2021) 3215–3220, <https://doi.org/10.1016/j.ccl.2021.03.064>.
- [13] N. Lu, X. Jing, Y. Xu, W. Lu, K. Liu, Z. Zhang, Effective cascade modulation of charge-carriers kinetics in the well-designed multi-component nanofiber system for highly-efficient photocatalytic H₂ generation, 2207045–0, Acta Phys. Chim. Sin. 0 (2022), <https://doi.org/10.3866/pku.whxb202207045>.
- [14] O. Carp, C.L. Huisman, A. Reller, Photoinduced reactivity of titanium dioxide, Prog. Solid State Chem. 32 (2004) 33–177, <https://doi.org/10.1016/j.progsolidstchem.2004.08.001>.
- [15] H. Lee, S.H. Park, S.J. Kim, B.H. Kim, H.S. Yoon, J.S. Kim, S.C. Jung, The effect of combined processes for advanced oxidation of organic dye using CVD TiO₂ film photo-catalysts, Prog. Org. Coat. 74 (2012) 758–763, <https://doi.org/10.1016/j.porgcoat.2011.09.024>.
- [16] F. Mastali Khan Tehrani, M. Rashidzadeh, A. Nemati, A. Irandoukht, B. Faridnia, Characterization and photocatalytic activities of nanosized titanium dioxide thin films, Int. J. Environ. Sci. Technol. 8 (2011) 545–552, <https://doi.org/10.1007/bf03326240>.
- [17] A. Kumar, A review on the factors affecting the photocatalytic degradation of hazardous materials, Mater. Sci. Eng. Int. J. 1 (2017) 1–10, <https://doi.org/10.15406/msei.2017.01.00018>.
- [18] Y. Lu, S. Guan, L. Hao, H. Yoshida, Review on the photocatalyst coatings of TiO₂: fabrication by mechanical coating technique and its application, Coatings 5 (2015) 425–464, <https://doi.org/10.3390/coatings5030425>.
- [19] A. Najafidoust, S. Allahyari, N. Rahemi, M. Tasbihi, Uniform coating of TiO₂ nanoparticles using biotemplates for photocatalytic wastewater treatment, Ceram. Int. 46 (2020) 4707–4719, <https://doi.org/10.1016/j.ceramint.2019.10.202>.
- [20] S. Sikdar, P.V. Menezes, R. Maccione, T. Jacob, P.L. Menezes, Plasma electrolytic oxidation (Peo) process—processing, properties, and applications, Nanomaterials 11 (2021) 1375, <https://doi.org/10.3390/nano11061375>.
- [21] E. Nikoomanzari, M. Karbasi, W.C.M.A. Melo, H. Moris, K. Babaei, S. Giannakis, A. Fattah-alhosseini, Impressive strides in antibacterial performance amelioration of Ti-based implants via plasma electrolytic oxidation (PEO): A review of the

- recent advancements, *Chem. Eng. J.* 441 (2022), 136003, <https://doi.org/10.1016/j.cej.2022.136003>.
- [22] A. Fattah-alhosseini, M. Molaei, K. Babaei, The effects of nano- and micro-particles on properties of plasma electrolytic oxidation (PEO) coatings applied on titanium substrates: A review, *Surf. Interfaces* 21 (2020), 100659, <https://doi.org/10.1016/j.surfin.2020.100659>.
- [23] T. Wang, H.-J. Wang, J.-S. Lin, J.-L. Yang, F.-L. Zhang, X.-M. Lin, Y.-J. Zhang, S. Jin, J.-F. Li, Plasmonic photocatalysis: mechanism, applications and perspectives, *Chin. J. Struct. Chem.* (2023), 100066, <https://doi.org/10.1016/j.cjsc.2023.100066>.
- [24] Y. Huang, Y. Yu, Y. Yu, B. Zhang, Oxygen vacancy engineering in photocatalysis, *Sol. RRL* 4 (2020) 1–14, <https://doi.org/10.1002/solr.202000037>.
- [25] X. Pan, M.Q. Yang, X. Fu, N. Zhang, Y.J. Xu, Defective TiO_2 with oxygen vacancies: synthesis, properties and photocatalytic applications, *Nanoscale* 5 (2013) 3601–3614, <https://doi.org/10.1039/c3nr00476g>.
- [26] H. Song, C. Li, Z. Lou, Z. Ye, L. Zhu, Effective Formation of Oxygen Vacancies in Black TiO_2 nanostructures with efficient solar-driven water splitting, *ACS Sustain. Chem. Eng.* 5 (2017) 8982–8987, <https://doi.org/10.1021/acssuschemeng.7b01774>.
- [27] H. Huang, S. Wang, Y. Zhang, P.K. Chu, Band gap engineering design for construction of energy-levels well-matched semiconductor heterojunction with enhanced visible-light-driven photocatalytic activity, *RSC Adv.* 40 (2014) 41219–41227, <https://doi.org/10.1039/c4ra05708b>.
- [28] A.G. Junior, A. Pereira, M. Gomes, M. Fraga, R. Pessoa, D. Leite, G. Petracconi, A. Nogueira, H. Wender, W. Miyakawa, M. Massi, A. da S. Sobrinho, Black TiO_2 thin films production using hollow cathode hydrogen plasma treatment: synthesis, material characteristics and photocatalytic activity, *Catalysts* 10 (2020) 282, <https://doi.org/10.3390/catal10030282>.
- [29] A. Naldoni, M. Alliati, S. Santangelo, M. Marelli, F. Fabbri, S. Cappelli, C. L. Bianchi, R. Psaro, V. Dal Santo, Effect of nature and location of defects on bandgap narrowing in black TiO_2 nanoparticles, *J. Am. Chem. Soc.* 134 (2012) 7600–7603, <https://doi.org/10.1021/ja3012676>.
- [30] Z. Hu, K. Li, X. Wu, N. Wang, X. Li, Q. Li, L. Li, K. Lv, Dramatic promotion of visible-light photoreactivity of TiO_2 hollow microspheres towards NO oxidation by introduction of oxygen vacancy, *Appl. Catal. B Environ.* 256 (2019), 117860, <https://doi.org/10.1016/j.apcatb.2019.117860>.
- [31] Y. Ding, Y. Wu, T. Zhang, L. Tao, X. Liu, X. Liu, L. Hu, T. Hayat, A. Alsaedi, S. Dai, Colorful TiO_{2-x} microspheres cooperating with titanium Schiff base complex for efficient visible light photocatalysts, *Catal. Today* 335 (2019) 550–556, <https://doi.org/10.1016/j.cattod.2019.03.004>.
- [32] H. Khatibinezhad, F. Ambriz-Vargas, F. Ben Ettouil, C. Moreau, An investigation on the photocatalytic activity of sub stoichiometric TiO_{2-x} coatings produced by suspension plasma spray, *J. Eur. Ceram. Soc.* 41 (2021) 544–556, <https://doi.org/10.1016/j.jeuceramsoc.2020.08.017>.
- [33] R. Katal, M. Salehi, M.H. Davood Abadi Farahani, S. Masudy-Panah, S.L. Ong, J. Hu, Preparation of a new type of black TiO_2 under a vacuum atmosphere for sunlight photocatalysis, *ACS Appl. Mater. Interfaces* 10 (2018) 35316–35326, <https://doi.org/10.1021/acsami.8b14680>.
- [34] X. Chen, L. Liu, P.Y. Yu, S.S. Mao, Increasing solar absorption for photocatalysis with black hydrogenated titanium dioxide nanocrystals, *Sci. (80-.)* 331 (2011) 746–750, <https://doi.org/10.1126/science.1200448>.
- [35] T. Leshuk, R. Parviz, P. Everett, H. Krishnakumar, R.A. Varin, F. Gu, Photocatalytic activity of hydrogenated TiO_2 , *ACS Appl. Mater. Interfaces* 5 (2013) 1892–1895, <https://doi.org/10.1021/am302903n>.
- [36] N. Liu, C. Schneider, D. Freitag, M. Hartmann, U. Venkatesan, J. Müller, E. Specker, P. Schmuki, Black TiO_2 nanotubes: Cocatalyst-free open-circuit hydrogen generation, *Nano Lett.* 14 (2014) 3309–3313, <https://doi.org/10.1021/nl500710j>.
- [37] S. Wei, R. Wu, X. Xu, J. Jian, H. Wang, Y. Sun, One-step synthetic approach for core-shell black anatase titania with high visible light photocatalytic performance, *Chem. Eng. J.* 299 (2016) 120–125, <https://doi.org/10.1016/j.cej.2016.04.067>.
- [38] Q. Wu, Q. Zheng, R. Van De Krol, Creating oxygen vacancies as a novel strategy to form tetrahedrally coordinated Ti^{4+} in Fe/TiO_2 nanoparticles, *J. Phys. Chem. C.* 116 (2012) 7219–7226, <https://doi.org/10.1021/jp212577g>.
- [39] A.M. Czoska, S. Livraghi, M. Chiesa, E. Giannello, S. Agnoli, G. Granozzi, E. Finazzi, C. Di Valentini, G. Pacchioni, The nature of defects in fluorine-doped TiO_2 , *J. Phys. Chem. C.* 112 (2008) 8951–8956, <https://doi.org/10.1021/jp8004184>.
- [40] Q. Kang, J. Cao, Y. Zhang, L. Liu, H. Xu, J. Ye, Reduced TiO_2 nanotube arrays for photoelectrochemical water splitting, *J. Mater. Chem. A* 1 (2013) 5766–5774, <https://doi.org/10.1039/c3ta01068f>.
- [41] D. Ariyanti, L. Mills, J. Dong, Y. Yao, W. Gao, NaBH_4 modified TiO_2 : defect site enhancement related to its photocatalytic activity, *Mater. Chem. Phys.* 199 (2017) 571–576, <https://doi.org/10.1016/j.matchemphys.2017.07.054>.
- [42] W. Fang, M. Xing, J. Zhang, A new approach to prepare Ti^{3+} self-doped TiO_2 via NaBH_4 reduction and hydrochloric acid treatment, *Appl. Catal. B Environ.* 160–161 (2014) 240–246, <https://doi.org/10.1016/j.apcatb.2014.05.031>.
- [43] J. Zhang, Y. Wang, J. Wu, X. Shu, C. Yu, J. Cui, Y. Qin, Y. Zhang, P.M. Ajayan, Y. Wu, Remarkable supercapacitive performance of TiO_2 nanotube arrays by introduction of oxygen vacancies, *Chem. Eng. J.* 313 (2017) 1071–1081, <https://doi.org/10.1016/j.cej.2016.11.004>.
- [44] R. Ren, Z. Wen, S. Cui, Y. Hou, X. Guo, J. Chen, Controllable synthesis and tunable photocatalytic properties of Ti^{3+} -doped TiO_2 , *Sci. Rep.* 5 (2015) 1–11, <https://doi.org/10.1038/srep10714>.
- [45] X.Q. Zhang, J.B. Chen, C.W. Wang, A.Z. Liao, X.F. Su, Low-temperature liquid phase reduced TiO_2 nanotube arrays: Synergy of morphology manipulation and oxygen vacancy doping for enhancement of field emission, *Nanotechnology* 26 (2015) 1–12, <https://doi.org/10.1088/0957-4484/26/17/175705>.
- [46] N.D. Diby, Y. Duan, P.A. Grah, F. Cai, Z. Yuan, Enhanced photoelectrochemical performance for hydrogen generation via introducing Ti^{3+} and oxygen vacancies into TiO_2 nanorod arrays, *J. Mater. Sci. Mater. Electron.* 29 (2018) 20236–20246, <https://doi.org/10.1007/s10854-018-0156-0>.
- [47] T. Lin, C. Yang, Z. Wang, H. Yin, X. Lü, F. Huang, J. Lin, X. Xie, M. Jiang, Effective nonmetal incorporation in black titania with enhanced solar energy utilization, *Energy Environ. Sci.* 7 (2014) 967–972, <https://doi.org/10.1039/c3ee42708k>.
- [48] M. Xing, W. Fang, M. Nasir, Y. Ma, J. Zhang, M. Anpo, Self-doped Ti^{3+} -enhanced TiO_2 nanoparticles with a high-performance photocatalysis, *J. Catal.* 297 (2013) 236–243, <https://doi.org/10.1016/j.jcat.2012.10.014>.
- [49] Y. Liu, B. Wei, L. Xu, H. Gao, M. Zhang, Generation of oxygen vacancy and OH radicals: a comparative study of Bi_2WO_6 and $\text{Bi}_2\text{WO}_{6-x}$ Nanoplates, *ChemCatChem* 7 (2015) 4076–4084, <https://doi.org/10.1002/cctc.201500714>.
- [50] P. Li, W. Cao, Y. Zhu, Q. Teng, L. Peng, C. Jiang, C. Feng, Y. Wang, NaOH-induced formation of 3D flower-sphere $\text{Bi}/\text{Br}/\text{Bi}_4\text{O}_3\text{Br}_2$ with proper-oxygen vacancies via in-situ self-template phase transformation method for antibiotic photodegradation, *Sci. Total Environ.* 715 (2020), 136809, <https://doi.org/10.1016/j.scitotenv.2020.136809>.
- [51] G. Li, W. Yang, S. Gao, Q. Shen, J. Xue, K. Chen, Q. Li, Creation of rich oxygen vacancies in bismuth molybdate nanosheets to boost the photocatalytic nitrogen fixation performance under visible light illumination, *Chem. Eng. J.* 404 (2021), 127115, <https://doi.org/10.1016/j.cej.2020.127115>.
- [52] J.S. Ma, M.C. Wen, C.H. Lu, Reaction mechanism and kinetics analysis of the phase transformation of TiO_2 from the anatase phase to the rutile phase, *J. Mater. Sci. Mater. Electron.* 24 (2013) 2506–2512, <https://doi.org/10.1007/s10854-013-1125-2>.
- [53] S. Chen, Y. Xiao, Y. Wang, Z. Hu, H. Zhao, W. Xie, A facile approach to prepare black TiO_2 with oxygen vacancy for enhancing photocatalytic activity, *Nanomaterials* 8 (2018) 245, <https://doi.org/10.3390/nano8040245>.
- [54] A. Ziarati, A. Badiei, R. Luque, Black hollow TiO_2 nanocubes: advanced nanoarchitectures for efficient visible light photocatalytic applications, *Appl. Catal. B Environ.* 238 (2018) 177–183, <https://doi.org/10.1016/j.apcatb.2018.07.020>.
- [55] X. Kang, X.Z. Song, Y. Han, J. Cao, Z. Tan, Defect-engineered TiO_2 hollow spiny nanocubes for phenol degradation under visible light irradiation, *Sci. Rep.* 8 (2018) 5904, <https://doi.org/10.1038/s41598-018-24353-8>.
- [56] J. Li, E.H. Wu, J. Hou, P. Huang, Z. Xu, Y. Jiang, Q.S. Liu, Y.Q. Zhong, A facile method for the preparation of black TiO_2 by Al reduction of TiO_2 and their visible light photocatalytic activity, *RSC Adv.* 10 (2020) 34775–34780, <https://doi.org/10.1039/dora06784a>.
- [57] W. Wang, C.H. Lu, Y.R. Ni, J. Bin Song, M.X. Su, Z.Z. Xu, Enhanced visible-light photoactivity of {001} facets dominated TiO_2 nanosheets with even distributed bulk oxygen vacancy and Ti^{3+} , *Catal. Commun.* 22 (2012) 19–23, <https://doi.org/10.1016/j.catcom.2012.02.011>.
- [58] M. Molaei, A. Fattah-alhosseini, M. Nouri, A. Nourian, Systematic optimization of corrosion, bioactivity, and biocompatibility behaviors of calcium-phosphate plasma electrolytic oxidation (PEO) coatings on titanium substrates, *Ceram. Int.* 48 (2022) 6322–6337, <https://doi.org/10.1016/j.ceramint.2021.11.175>.
- [59] Y. Yang, T. Sun, F. Ma, L.F. Huang, Z. Zeng, Superhydrophilic Fe^{3+} -Doped TiO_2 films with long-lasting antifogging performance, *ACS Appl. Mater. Interfaces* 13 (2021) 3377–3386, <https://doi.org/10.1021/acsami.0c18444>.
- [60] M.S. Hosseini, M.T. Sadeghi, M. Khazaei, Improving oleophobicity and hydrophilicity of superhydrophobic surface by TiO_2 -based coatings, *Mater. Res. Express* 5 (2018), 08510, <https://doi.org/10.1088/2053-1591/aa2b8>.
- [61] M.E. Simonsen, Z. Li, E.G. Søgaard, Influence of the OH groups on the photocatalytic activity and photoinduced hydrophilicity of microwave assisted sol-gel TiO_2 film, *Appl. Surf. Sci.* 255 (2009) 8054–8062, <https://doi.org/10.1016/j.apsusc.2009.05.013>.
- [62] G.W. Lin, J.S. Chen, W. Tseng, F.H. Lu, Formation of anatase TiO_2 coatings by plasma electrolytic oxidation for photocatalytic applications, *Surf. Coat. Technol.* 357 (2019) 28–35, <https://doi.org/10.1016/j.surcoat.2018.10.010>.
- [63] S. Stojadinović, N. Radić, N. Tadić, R. Vasilić, A. Tsanov, $\text{TiO}_2/\text{Bi}_2\text{O}_3$ coatings formed by plasma electrolytic oxidation of titanium for photocatalytic applications, *J. Mater. Sci. Mater. Electron.* 33 (2022) 4467–4481, <https://doi.org/10.1007/s10854-021-07637-0>.
- [64] A. Hoseini, B. Yarmand, Immobilization of $\text{Fe}_2\text{O}_3/\text{TiO}_2$ photocatalyst on the metallic substrate via plasma electrolytic oxidation process: degradation efficiency, *J. Nanopart. Res.* 22 (2020), <https://doi.org/10.1007/s11051-020-05043-x>.
- [65] P. Manojkumar, E. Lokeshkumar, A. Saikiran, B. Govardhanan, M. Ashok, N. Rameshbabu, Visible light photocatalytic activity of metal (Mo/V/W) doped porous TiO_2 coating fabricated on Cp-Ti by plasma electrolytic oxidation, *J. Alloy. Compd.* 825 (2020), 154092, <https://doi.org/10.1016/j.jallcom.2020.154092>.
- [66] M.R. Bayati, R. Molaei, Visible photoinduced hydrophilicity of $\text{V}_2\text{O}_5-\text{TiO}_2$ nanoporous ceramic layers grown via micro-arc oxidation, *J. Phys. D. Appl. Phys.* 43 (2010), 505304, <https://doi.org/10.1088/0022-3727/43/50/505304>.
- [67] Z. Li, H. Bian, X. Xiao, J. Shen, C. Zhao, J. Lu, Y.Y. Li, Defective Black TiO_2 nanotube arrays for enhanced photocatalytic and photoelectrochemical applications, *ACS Appl. Nano Mater.* 2 (2019) 7372–7378, <https://doi.org/10.1021/acsnanm.9b01878>.

- [68] J. Gao, J. Xue, S. Jia, Q. Shen, X. Zhang, H. Jia, X. Liu, Q. Li, Y. Wu, Self-doping surface oxygen vacancy-induced lattice strains for enhancing visible light-driven photocatalytic H_2 evolution over black TiO_2 , *ACS Appl. Mater. Interfaces* 13 (2021) 18758–18771, <https://doi.org/10.1021/acsami.1c01101>.
- [69] P. Manojkumar, E. Lokeshkumar, C. Premchand, A. Saikiran, L. Rama Krishna, N. Rameshbabu, Facile preparation of immobilized visible light active $W-TiO_2/rGO$ composite photocatalyst by plasma electrolytic oxidation process, *Phys. B Condens. Matter* 631 (2022), 413680, <https://doi.org/10.1016/j.physb.2022.413680>.
- [70] S. Stojadinović, N. Radić, R. Vasilčić, M. Petković, P. Stefanov, L. Žeković, B. Grbić, Photocatalytic properties of TiO_2/WO_3 coatings formed by plasma electrolytic oxidation of titanium in 12-tungstosilicic acid, *Appl. Catal. B Environ.* 126 (2012) 334–341, <https://doi.org/10.1016/j.apcatb.2012.07.031>.
- [71] L. Kurnazhitksy, V. Shymanova, T. Gavrilko, V. Naumov, L. Fedorenko, V. Kshnyakin, J. Baran, Photoluminescence of Cr-doped TiO_2 induced by intense UV laser excitation, *J. Lumin.* 166 (2015) 253–258, <https://doi.org/10.1016/j.jlumin.2015.03.034>.
- [72] P.A. Bharad, A.V. Nikam, F. Thomas, C.S. Gopinath, CuO_x-TiO_2 composites: electronically integrated nanocomposites for solar hydrogen generation, *ChemistrySelect* 3 (2018) 12022–12030, <https://doi.org/10.1002/slct.201802047>.
- [73] L. Chetibi, T. Busko, N.P. Kulish, D. Hamana, S. Chaieb, S. Achour, Photoluminescence properties of TiO_2 nanofibers, *J. Nanopart. Res.* 19 (2017) 129, <https://doi.org/10.1007/s11051-017-3822-x>.
- [74] S. Wu, X. Li, Y. Tian, Y. Lin, Y.H. Hu, Excellent photocatalytic degradation of tetracycline over black anatase- TiO_2 under visible light, *Chem. Eng. J.* 406 (2021), 126747, <https://doi.org/10.1016/j.cej.2020.126747>.
- [75] M. Ji, Y.H. Choa, Y.I. Lee, One-step synthesis of black TiO_{2-x} microspheres by ultrasonic spray pyrolysis process and their visible-light-driven photocatalytic activities, *Ultrason. Sonochem.* 74 (2021), 105557, <https://doi.org/10.1016/j.ultrsonch.2021.105557>.
- [76] J. Li, M. Zhang, Z. Guan, Q. Li, C. He, J. Yang, Synergistic effect of surface and bulk single-electron-trapped oxygen vacancy of TiO_2 in the photocatalytic reduction of CO_2 , *Appl. Catal. B Environ.* 206 (2017) 300–307, <https://doi.org/10.1016/j.apcatb.2017.01.025>.
- [77] S. Bai, N. Zhang, C. Gao, Y. Xiong, Defect engineering in photocatalytic materials, *Nano Energy* 53 (2018) 296–336, <https://doi.org/10.1016/j.nanoen.2018.08.058>.
- [78] H. Tan, Z. Zhao, M. Niu, C. Mao, D. Cao, D. Cheng, P. Feng, Z. Sun, A facile and versatile method for preparation of colored TiO_2 with enhanced solar-driven photocatalytic activity, *Nanoscale* 6 (2014) 10216–10223, <https://doi.org/10.1039/c4nr02677b>.
- [79] X. Sun, J. Ming, Q. Ma, C. Zhang, Y. Zhu, G. An, G. Chen, Y. Yang, Fabrication of optimal oxygen vacancy amount in $P/Ag/Ag_2O/Ag_3PO_4/TiO_2$ through a green photoreduction process for sustainable H_2 evolution under solar light, *J. Colloid Interface Sci.* 645 (2023) 176–187, <https://doi.org/10.1016/j.jcis.2023.04.085>.
- [80] J.H. Kim, Y.J. Jang, J.H. Kim, J.W. Jang, S.H. Choi, J.S. Lee, Defective $ZnFe_2O_4$ nanorods with oxygen vacancy for photoelectrochemical water splitting, *Nanoscale* 7 (2015) 19144–19151, <https://doi.org/10.1039/c5nr05812k>.
- [81] S. Jia, J. Gao, Q. Shen, J. Xue, Z. Zhang, X. Liu, H. Jia, Effect of oxygen vacancy concentration on the photocatalytic hydrogen evolution performance of anatase TiO_2 : DFT and experimental studies, *J. Mater. Sci. Mater. Electron.* 32 (2021) 13369–13381, <https://doi.org/10.1007/s10854-021-05915-5>.
- [82] M. Molaei, A. Fattah-alhosseini, M. Nouri, P. Mahmoodi, A. Nourian, Incorporating TiO_2 nanoparticles to enhance corrosion resistance, cytocompatibility, and antibacterial properties of PEO ceramic coatings on titanium, *Ceram. Int.* 48 (2022) 21005–21024, <https://doi.org/10.1016/j.ceramint.2022.04.096>.
- [83] M. Alifkhazraei, D.D. Macdonald, E. Matykina, E.V. Parfenov, V.S. Egorkin, J. A. Curran, S.C. Troughton, S.L. Sinebryukhov, S.V. Gnedenvkov, T. Lampke, F. Simchen, H.F. Nabavi, Review of plasma electrolytic oxidation of titanium substrates: Mechanism, properties, applications and limitations, *Appl. Surf. Sci. Adv.* 5 (2021), 100121, <https://doi.org/10.1016/j.apsadv.2021.100121>.
- [84] A. Santos-Coquillat, M. Mohedano, E. Martinez-Campos, R. Arrabal, A. Pardo, E. Matykina, Bioactive multi-elemental PEO-coatings on titanium for dental implant applications, *Mater. Sci. Eng. C*. 97 (2019) 738–752, <https://doi.org/10.1016/j.msec.2018.12.097>.
- [85] S. Ebrahimi, A. Bordbar-Khiabani, B. Yarmand, M.A. Asghari, Improving optoelectrical properties of photoactive anatase TiO_2 coating using rGO incorporation during plasma electrolytic oxidation, *Ceram. Int.* 45 (2019) 1746–1754, <https://doi.org/10.1016/j.ceramint.2018.10.057>.
- [86] H. Wu, L. Xie, M. He, R. Zhang, Y. Tian, S. Liu, T. Gong, F. Huo, T. Yang, Q. Zhang, S. Guo, W. Tian, A wear-resistant TiO_2 nanoceramic coating on titanium implants for visible-light photocatalytic removal of organic residues, *Acta Biomater.* 97 (2019) 597–607, <https://doi.org/10.1016/j.actbio.2019.08.009>.
- [87] C. Zhao, Y. Yang, L. Luo, S. Shao, Y. Zhou, Y. Shao, F. Zhan, J. Yang, Y. Zhou, γ -ray induced formation of oxygen vacancies and Ti^{3+} defects in anatase TiO_2 for efficient photocatalytic organic pollutant degradation, *Sci. Total Environ.* 747 (2020), 141533, <https://doi.org/10.1016/j.scitotenv.2020.141533>.
- [88] L. Si, Z. Huang, K. Lv, D. Tang, C. Yang, Facile preparation of Ti^{3+} -self-doped TiO_2 nanosheets with dominant {0 0 1} facets using zinc powder as reductant, *J. Alloy. Compd.* 601 (2014) 88–93, <https://doi.org/10.1016/j.jallcom.2014.02.141>.
- [89] J. Pan, Z. Dong, B. Wang, Z. Jiang, C. Zhao, J. Wang, C. Song, Y. Zheng, C. Li, The enhancement of photocatalytic hydrogen production via Ti^{3+} self-doping black $TiO_2/g-C_3N_4$ hollow core-shell nano-heterojunction, *Appl. Catal. B Environ.* 242 (2019) 92–99, <https://doi.org/10.1016/j.apcatb.2018.09.079>.
- [90] M. Shen, M. Wang, Q. Wang, J. Tian, L. Zhang, L. Wang, J. Shi, A Ti-OH bond breaking route for creating oxygen vacancy in titania towards efficient CO_2 photoreduction, *Chem. Eng. J.* 425 (2021), 131513, <https://doi.org/10.1016/j.cej.2021.131513>.
- [91] Q. Cheng, A. Wang, Z. Song, J. Bao, J. Xue, Y. Wei, S. Li, L. Lv, J. Ding, M. Cai, J. Chen, Q. Wang, C. Gao, S. Sun, Enhancement and stabilization of isolated hydroxyl groups via the construction of coordinatively unsaturated sites on surface and subsurface of hydrogenated TiO_2 nanotube arrays for photocatalytic complete mineralization of toluene, *J. Environ. Chem. Eng.* 9 (2021), 105080, <https://doi.org/10.1016/j.je.2021.105080>.
- [92] D. He, Y. Sun, L. Xin, J. Feng, Aqueous tetracycline degradation by non-thermal plasma combined with nano- TiO_2 , *Chem. Eng. J.* 258 (2014) 18–25, <https://doi.org/10.1016/j.cej.2014.07.089>.
- [93] Z. Fang, H. Jiang, J. Gong, H. Zhang, X. Hu, K. Ouyang, Y. Guo, X. Hu, H. Wang, P. Wang, Removal of tetracycline hydrochloride from water by visible-light photocatalysis using $BiFeO_3/BC$ materials, *Catalysts* 12 (2022) 1461, <https://doi.org/10.3390/catal12111461>.
- [94] H. Zhang, J. Li, X. He, B. Liu, Preparation of a $g-C_3N_4/Uio-66-NH_2/CdS$ photocatalyst with enhanced visible light photocatalytic activity for tetracycline degradation, *Nanomaterials* 10 (2020) 1–14, <https://doi.org/10.3390/nano10091824>.
- [95] C. Zhou, C. Lai, P. Xu, G. Zeng, D. Huang, Z. Li, C. Zhang, M. Cheng, L. Hu, J. Wan, F. Chen, W. Xiong, R. Deng, Rational design of carbon-doped carbon nitride/ $Bi_{12}O_7Cl_2$ composites: a promising candidate photocatalyst for boosting visible-light-driven photocatalytic degradation of tetracycline, *ACS Sustain. Chem. Eng.* 6 (2018) 6941–6949, <https://doi.org/10.1021/acssuschemeng.8b00782>.
- [96] B. Kakavandi, N. Bahari, R. Rezaei Kalantary, E. Dehghani Fard, Enhanced sonophotocatalysis of tetracycline antibiotic using TiO_2 decorated on magnetic activated carbon (MAC@T) coupled with US and UV: a new hybrid system, *Ultrason. Sonochem.* 55 (2019) 75–85, <https://doi.org/10.1016/j.ultrsonch.2019.02.026>.
- [97] N. Belhouchet, B. Hamdi, H. Chenchouni, Y. Bessekhouad, Photocatalytic degradation of tetracycline antibiotic using new calcite/titania nanocomposites, *J. Photochem. Photobiol. A* 372 (2019) 196–205, <https://doi.org/10.1016/j.jphotochem.2018.12.016>.
- [98] M. Karbasi, E. Nikoomanzari, R. Hosseini, H. Bahramian, R. Chaharmahali, S. Giannakis, M. Kaseem, A. Fattah-alhosseini, A review on plasma electrolytic oxidation coatings for organic pollutant degradation: how to prepare them and what to expect of them? *J. Environ. Chem. Eng.* 11 (2023), 110027 <https://doi.org/10.1016/j.jece.2023.110027>.
- [99] M. Kohantobri, G. Moussavi, P. Oulego, S. Giannakis, Radical-based degradation of sulfamethoxazole via UVA/PMS-assisted photocatalysis, driven by magnetically separable $Fe_3O_4@CeO_2/BiO$ nanospheres, *Sep. Purif. Technol.* 267 (2021), 118665, <https://doi.org/10.1016/j.seppur.2021.118665>.
- [100] M.A. Haki, A. Imgharn, N. Araab, A. Hsini, A. Essekri, M. Laab, H. El Jazouli, M. Elamine, R. Lakhmiri, A. Albourine, Efficient removal of crystal violet dye from aqueous solutions using sodium hydroxide-modified avocado shells: kinetics and isotherms modeling, *Water Sci. Technol.* 85 (2022) 433–448, <https://doi.org/10.2166/wst.2021.451>.
- [101] J.J. Gulicovski, L.S. Čerović, S.K. Milonjić, Point of zero charge and isoelectric point of alumina, *Mater. Manuf. Process.* 23 (2008) 615–619, <https://doi.org/10.1080/10426910802160668>.
- [102] Y. Zhao, J. Geng, X. Wang, X. Gu, S. Gao, Tetracycline adsorption on kaolinite: PH, metal cations and humic acid effects, *Ecotoxicology* 20 (2011) 1141–1147, <https://doi.org/10.1007/s10646-011-0665-6>.
- [103] G. Gopal, S.A. Alex, N. Chandrasekaran, A. Mukherjee, A review on tetracycline removal from aqueous systems by advanced treatment techniques, *RSC Adv.* 10 (2020) 27081–27095, <https://doi.org/10.1039/dora04264a>.
- [104] W. Subramonian, T.Y. Wu, Effect of enhancers and inhibitors on photocatalytic sunlight treatment of methylene blue, *Water Air. Soil Pollut.* 225 (2014) 1922, <https://doi.org/10.1007/s11270-014-1922-0>.
- [105] X. Wang, J. Jia, Y. Wang, Combination of photocatalysis with hydrodynamic cavitation for degradation of tetracycline, *Chem. Eng. J.* 315 (2017) 274–282, <https://doi.org/10.1016/j.cej.2017.01.011>.
- [106] K. Guan, Relationship between photocatalytic activity, hydrophilicity and self-cleaning effect of TiO_2/SiO_2 films, *Surf. Coat. Technol.* 191 (2005) 155–160, <https://doi.org/10.1016/j.surcoa.2004.02.022>.
- [107] X. Xin, T. Xu, L. Wang, C. Wang, Ti^{3+} -self doped brookite TiO_2 single-crystalline nanosheets with high solar absorption and excellent photocatalytic CO_2 reduction, *Sci. Rep.* 6 (2016) 1–8, <https://doi.org/10.1038/srep23684>.
- [108] Y. Li, Z. Ren, M. Gu, Y. Duan, W. Zhang, K. Lv, Synergistic effect of interstitial C doping and oxygen vacancies on the photoreactivity of TiO_2 nanofibers towards CO_2 reduction, *Appl. Catal. B Environ.* 317 (2022), 121773, <https://doi.org/10.1016/j.apcatb.2022.121773>.
- [109] M. Karbasi, S.J. Hashemifar, F. Karimzadeh, S. Giannakis, C. Pulgarin, K. Raeissi, A. Sienkiewicz, Decrypting the photocatalytic bacterial inactivation of hierarchical flower-like Bi_2WO_6 microspheres induced by surface properties: experimental studies and ab initio calculations, *Chem. Eng. J.* 427 (2022), 131768, <https://doi.org/10.1016/j.cej.2021.131768>.
- [110] Y. Cao, Z. Xing, Y. Shen, Z. Li, X. Wu, X. Yan, J. Zou, S. Yang, W. Zhou, Mesoporous black $Ti^{3+}/N-TiO_2$ spheres for efficient visible-light-driven photocatalytic performance, *Chem. Eng. J.* 325 (2017) 199–207, <https://doi.org/10.1016/j.cej.2017.05.080>.

- [111] D.A. Torres-Ceron, E. Restrepo-Parra, C.D. Acosta-Medina, D. Escobar-Rincon, R. Ospina-Ospina, Study of duty cycle influence on the band gap energy of TiO_2/P coatings obtained by PEO process, *Surf. Coat. Technol.* 375 (2019) 221–228, <https://doi.org/10.1016/j.surfcot.2019.06.021>.
- [112] D.A. Torres-Ceron, S. Amaya-Roncancio, J.S. Riva, A. Vargas-Eudor, D. Escobar-Rincon, E. Restrepo-Parra, Incorporation of P^{3+} and P^{5-} from phosphate precursor in TiO_2/P coatings produced by PEO: XPS and DFT study, *Surf. Coat. Technol.* 421 (2021), 127437, <https://doi.org/10.1016/j.surfcot.2021.127437>.
- [113] S. Shalini, R. Balasundaraprabhu, T. Sathish Kumar, N. Muthukumarasamy, S. Prasanna, K. Sivakumaran, M.D. Kannan, Enhanced performance of sodium doped TiO_2 nanorods based dye sensitized solar cells sensitized with extract from petals of Hibiscus sabdariffa (Roselle), *Mater. Lett.* 221 (2018) 192–195, <https://doi.org/10.1016/j.matlet.2018.03.091>.
- [114] B. Han, Y.H. Hu, Highly efficient temperature-induced visible light photocatalytic hydrogen production from water, *J. Phys. Chem. C* 119 (2015) 18927–18934, <https://doi.org/10.1021/acs.jpcc.5b04894>.
- [115] T.S. Rajaraman, S.P. Parikh, V.G. Gandhi, Black TiO_2 : a review of its properties and conflicting trends, *Chem. Eng. J.* 389 (2020), <https://doi.org/10.1016/j.cej.2019.123918>.
- [116] X. Xin, T. Xu, J. Yin, L. Wang, C. Wang, Management on the location and concentration of Ti^{3+} in anatase TiO_2 for defects-induced visible-light photocatalysis, *Appl. Catal. B Environ.* 176–177 (2015) 354–362, <https://doi.org/10.1016/j.apcatb.2015.04.016>.
- [117] H. Salari, M. Kohantorabi, Fabrication of novel $\text{Fe}_2\text{O}_3/\text{MoO}_3/\text{AgBr}$ nanocomposites with enhanced photocatalytic activity under visible light irradiation for organic pollutant degradation, *Adv. Powder Technol.* 31 (2020) 493–503, <https://doi.org/10.1016/j.japt.2019.11.005>.
- [118] H. Salari, M. Kohantorabi, Heterogeneous photocatalytic degradation of organic pollutant in aqueous solutions by S-scheme heterojunction in nickel molybdate nanocomposites, *J. Environ. Chem. Eng.* 9 (2021), 105903, <https://doi.org/10.1016/j.jece.2021.105903>.
- [119] M. Kohantorabi, G. Moussavi, S. Mohammadi, P. Oulego, S. Giannakis, Photocatalytic activation of peroxymonosulfate (PMS) by novel mesoporous $\text{Ag}/\text{ZnO}@\text{NiFe}_2\text{O}_4$ nanorods, inducing radical-mediated acetaminophen degradation under UVA irradiation, *Chemosphere* 277 (2021), 130271, <https://doi.org/10.1016/j.chemosphere.2021.130271>.
- [120] J. Ni, W. Wang, D. Liu, Q. Zhu, J. Jia, J. Tian, Z. Li, X. Wang, Z. Xing, Oxygen vacancy-mediated sandwich-structural TiO_{2-x} /ultrathin $\text{g}-\text{C}_3\text{N}_4/\text{TiO}_{2-x}$ direct Z-scheme heterojunction visible-light-driven photocatalyst for efficient removal of high toxic tetracycline antibiotics, *J. Hazard. Mater.* 408 (2021), 124432, <https://doi.org/10.1016/j.jhazmat.2020.124432>.
- [121] E. Prabakaran, T. Velempini, M. Molefe, K. Pillay, Comparative study of KF, KCl and KBr doped with graphitic carbon nitride for superior photocatalytic degradation of methylene blue under visible light, *J. Mater. Res. Technol.* 15 (2021) 6340–6355, <https://doi.org/10.1016/j.jmrt.2021.10.128>.
- [122] R. Shen, L. Hao, Q. Chen, Q. Zheng, P. Zhang, X. Li, P-Doped $\text{g}-\text{C}_3\text{N}_4$ nanosheets with highly dispersed $\text{Co}_{0.2}\text{Ni}_{1.6}\text{Fe}_{0.2}\text{P}$ cocatalyst for efficient photocatalytic hydrogen evolution, *Wuli Huaxue Xuebao/ Acta Phys. - Chim. Sin.* 38 (2022) 1–10, <https://doi.org/10.3866/PKU.WHXB202110014>.
- [123] J. Lim, Y. Yang, M.R. Hoffmann, Activation of peroxymonosulfate by oxygen vacancies-enriched cobalt-doped black TiO_2 nanotubes for the removal of organic pollutants, *Environ. Sci. Technol.* 53 (2019) 6972–6980, <https://doi.org/10.1021/acs.est.9b01449>.
- [124] A.O. Oluwole, O.S. Olatunji, Photocatalytic degradation of tetracycline in aqueous systems under visible light irradiation using needle-like SnO_2 nanoparticles anchored on exfoliated $\text{g}-\text{C}_3\text{N}_4$, *Environ. Sci. Eur.* 34 (2022) 5, <https://doi.org/10.1186/s12302-021-00588-7>.
- [125] D. Wang, S. Li, Q. Feng, Supramolecular self-assembled carbon nitride for the degradation of tetracycline hydrochloride, *J. Mater. Sci. Mater. Electron.* 29 (2018) 9380–9386, <https://doi.org/10.1007/s10854-018-8970-y>.
- [126] J. Huang, H. Zhang, Mn-based catalysts for sulfate radical-based advanced oxidation processes: a review, *Environ. Int.* 133 (2019), 105141, <https://doi.org/10.1016/j.envint.2019.105141>.
- [127] S. Wang, Z. Zhou, R. Zhou, Z. Fang, P.J. Cullen, Highly synergistic effect for tetracycline degradation by coupling a transient spark gas-liquid discharge with TiO_2 photocatalysis, *Chem. Eng. J.* 450 (2022), 138409, <https://doi.org/10.1016/j.cej.2022.138409>.
- [128] C.Y. Pei, Y.G. Chen, L. Wang, W. Chen, G.B. Huang, Step-scheme $\text{WO}_3/\text{CdIn}_2\text{S}_4$ hybrid system with high visible light activity for tetracycline hydrochloride photodegradation, *Appl. Surf. Sci.* 535 (2021), 147682, <https://doi.org/10.1016/j.apsusc.2020.147682>.
- [129] X.D. Zhu, Y.J. Wang, R.J. Sun, D.M. Zhou, Photocatalytic degradation of tetracycline in aqueous solution by nanosized TiO_2 , *Chemosphere* 92 (2013) 925–932, <https://doi.org/10.1016/j.chemosphere.2013.02.066>.
- [130] Q. Zhang, L. Jiang, J. Wang, Y. Zhu, Y. Pu, W. Dai, Photocatalytic degradation of tetracycline antibiotics using three-dimensional network structure perylene diimide supramolecular organic photocatalyst under visible-light irradiation, *Appl. Catal. B Environ.* 277 (2020), 119122, <https://doi.org/10.1016/j.apcatb.2020.119122>.
- [131] F. Al Momani, C. Sans, S. Esplugas, A comparative study of the advanced oxidation of 2,4-dichlorophenol, *J. Hazard. Mater.* 107 (2004) 123–129, <https://doi.org/10.1016/j.jhazmat.2003.11.015>.
- [132] S. Contreras, M. Rodríguez, F. Al Momani, C. Sans, S. Esplugas, Contribution of the ozonation pre-treatment to the biodegradation of aqueous solutions of 2,4-dichlorophenol, *Water Res* 37 (2003) 3164–3171, [https://doi.org/10.1016/S0043-1354\(03\)00167-2](https://doi.org/10.1016/S0043-1354(03)00167-2).
- [133] M. Karbasi, F. Karimzadeh, K. Raeissi, S. Giannakis, C. Pulgarin, Improving visible light photocatalytic inactivation of *E. coli* by inducing highly efficient radical pathways through peroxymonosulfate activation using 3-D, surface-enhanced, reduced graphene oxide (rGO) aerogels, *Chem. Eng. J.* 396 (2020), 125189, <https://doi.org/10.1016/j.cej.2020.125189>.
- [134] Y. Nosaka, A.Y. Nosaka, Generation and detection of reactive oxygen species in photocatalysis, *Chem. Rev.* 117 (2017) 11302–11336, <https://doi.org/10.1021/crrev.7b00161>.
- [135] J. Rodríguez-Chueca, E. Alonso, D.N. Singh, Photocatalytic mechanisms for peroxymonosulfate activation through the removal of methylene blue: A case study, *Int. J. Environ. Res. Public Health* 16 (2019) 198, <https://doi.org/10.3390/ijerph16020198>.
- [136] J. Cao, L. Lai, B. Lai, G. Yao, X. Chen, L. Song, Degradation of tetracycline by peroxymonosulfate activated with zero-valent iron: Performance, intermediates, toxicity and mechanism, *Chem. Eng. J.* 364 (2019) 45–56, <https://doi.org/10.1016/j.cej.2019.01.113>.
- [137] W. Da Oh, Z. Dong, T.T. Lin, Generation of sulfate radical through heterogeneous catalysis for organic contaminants removal: Current development, challenges and prospects, *Appl. Catal. B Environ.* 194 (2016) 169–201, <https://doi.org/10.1016/j.apcatb.2016.04.003>.
- [138] Z.J. Xiao, X.C. Feng, H.T. Shi, B.Q. Zhou, W.Q. Wang, N.Q. Ren, Why the cooperation of radical and non-radical pathways in PMS system leads to a higher efficiency than a single pathway in tetracycline degradation, *J. Hazard. Mater.* 424 (2022), 127247, <https://doi.org/10.1016/j.jhazmat.2021.127247>.
- [139] C. Zhu, Y. Zhang, Z. Fan, F. Liu, A. Li, Carbonate-enhanced catalytic activity and stability of Co_3O_4 nanowires for O_2 -driven bisphenol A degradation via peroxymonosulfate activation: Critical roles of electron and proton acceptors, *J. Hazard. Mater.* 393 (2020), 122395, <https://doi.org/10.1016/j.jhazmat.2020.122395>.
- [140] S. Mohammadi, G. Moussavi, S. Shekoohiyan, M.L. Marín, F. Boscá, S. Giannakis, A continuous-flow catalytic process with natural hematite-alginate beads for effective water decontamination and disinfection: Peroxymonosulfate activation leading to dominant sulfate radical and minor non-radical pathways, *Chem. Eng. J.* 411 (2021), 127738, <https://doi.org/10.1016/j.cej.2020.127738>.
- [141] S. Shanavas, A. Priyadharsan, E.I. Gkanas, R. Acevedo, P.M. Anbarasan, High efficient catalytic degradation of tetracycline and ibuprofen using visible light driven novel $\text{Cu}/\text{Bi}_2\text{Ti}_2\text{O}_7/\text{rGO}$ nanocomposite: Kinetics, intermediates and mechanism, *J. Ind. Eng. Chem.* 72 (2019) 512–528, <https://doi.org/10.1016/j.jiec.2019.01.008>.
- [142] H. Huang, T. Guo, K. Wang, Y. Li, G. Zhang, Efficient activation of persulfate by a magnetic recyclable pomegranate seed biochar catalyst for the degradation of tetracycline hydrochloride in water, *Sci. Total Environ.* 758 (2021), 143957, <https://doi.org/10.1016/j.scitotenv.2020.143957>.
- [143] J. Cao, S. Sun, X. Li, Z. Yang, W. Xiong, Y. Wu, M. Jia, Y. Zhou, C. Zhou, Y. Zhang, Efficient charge transfer in aluminum-cobalt layered double hydroxide derived from Co-ZIF for enhanced catalytic degradation of tetracycline through peroxymonosulfate activation, *Chem. Eng. J.* 382 (2020), 122802, <https://doi.org/10.1016/j.cej.2019.122802>.
- [144] F. Liu, J. Cao, Z. Yang, W. Xiong, Z. Xu, P. Song, M. Jia, S. Sun, Y. Zhang, X. Zhong, Heterogeneous activation of peroxymonosulfate by cobalt-doped MIL-53(Al) for efficient tetracycline degradation in water: coexistence of radical and non-radical reactions, *J. Colloid Interface Sci.* 581 (2021) 195–204, <https://doi.org/10.1016/j.jcis.2020.07.100>.